Science Advances
AAAS

Title

Critical soil moisture thresholds of plant water stress in terrestrial ecosystems

Authors

Zheng Fu[1]*, Philippe Ciais[1], Andrew F. Feldman[2], Pierre Gentine[3], David Makowski[4], I. Colin Prentice[5, 6], Paul C. Stoy[7], Ana Bastos[8], Jean-Pierre Wigneron[9]

Affiliations

[1] Laboratoire des Sciences du Climat et de l'Environnement, LSCE/IPSL, CEA-CNRS-UVSQ, Université Paris-Saclay, Gif-sur-Yvette, 91191, France

[2] NASA Goddard Space Flight Center, Earth Sciences Division, Greenbelt, MD 20771, USA

[3] Department of Earth and Environmental Engineering, Columbia University, New York, NY, 10027, USA

[4] Unit Applied mathematics and computer science (UMR 518) INRAE AgroParisTech Université Paris-Saclay, Paris, France

[5] Georgina Mace Centre for the Living Planet, Department of Life Sciences, Imperial College London, Silwood Park Campus, Buckhurst Road, Ascot, SL5 7PY, UK

[6] Ministry of Education Key Laboratory for Earth System Modeling, Department of Earth System Science, Tsinghua University, Beijing 100084, China

[7] Department of Biological Systems Engineering, University of Wisconsin – Madison, USA

[8] Department Biogeochemical Integration, Max Planck Institute for Biogeochemistry, D-07745 Jena, Germany

[9] ISPA, INRAE, Université de Bordeaux, Bordeaux Sciences Agro, F-33140, Villenave d'Ornon, France

*Correspondence author: zheng.fu@lsce.ipsl.fr

Abstract

Plant water stress occurs at the point when soil moisture (SM) limits transpiration, defining a critical SM threshold (θ_{crit}). Knowledge of the spatial distribution of θ_{crit} is crucial for future projections of climate and water resources, food production, and ecosystem vulnerability. Here, we use global eddy-covariance observations to quantify θ_{crit} and evaporative fraction (EF) regimes during dry-downs. Three canonical variables describe how EF is controlled by SM: the maximum EF (EF_{max}), θ_{crit}, and the slope (S) between EF and SM below θ_{crit}. We find systematic differences of these three variables across biomes. Variation in θ_{crit}, S, and EF_{max} is mostly explained by soil texture, vapor pressure deficit and precipitation, respectively, while vegetation structure also plays an influential role. Dryland ecosystems such as savannas, operate at low θ_{crit} and show adaptation to water deficits. The negative relationship between θ_{crit} and S indicates that dryland ecosystems minimize θ_{crit} through mechanisms of sustained SM extraction and transport by xylem. Our results further suggest an optimal adaptation of local EF–SM response function, that maximizes growing-season evapotranspiration and photosynthesis.

Teaser

Defined new observational thresholds of plant water stress and their environmental drivers.

Introduction

The critical soil moisture (SM) threshold (θ_{crit}) of plant water stress occurs near the point when evapotranspiration becomes SM limited (*1*). Below this threshold, a marginal reduction of SM leads to reduced evapotranspiration and increased sensible heat flux (*2*). Crossing this threshold results into decreased evaporative fraction (EF), the ratio of latent heat to the sum of latent and sensible heat fluxes, making the air above the canopy warmer and drier, which in turn further reduces transpiration and plant carbon dioxide uptake (*3-5*). The existence of critical SM thresholds plays a crucial role in the surface energy partitioning (*6-8*). SM-controlled energy partitioning determines local climate and land-atmosphere coupling, and can amplify warming in transition regions (*9, 10*). A better knowledge of critical SM thresholds is also important to assess crop yield risks and ecosystem vulnerability from drought exposure (*7*).

The land surface hydrology community has historically observed that the θ_{crit} level at which water-limitation of evapotranspiration begins is above the SM wilting point of extreme stress (*7*). Yet, it is not clear if plant photosynthetic processes become water-stressed at the same θ_{crit} as evapotranspiration. For evapotranspiration, the θ_{crit} can be quantified by evaluating the EF–SM relationship (*2, 5, 8, 11, 12*). For photosynthesis, the onset of water stress at ecosystem level was found to correspond to the SM critical value at which the sign of the covariance between daily gross primary production (GPP) and vapor pressure deficit (VPD) switches from a positive to negative sign when SM decreases during a soil drying period (*13*). GPP and evapotranspiration are tightly coupled on short time scales (*4*) and VPD combines the effects of both water stress and energy demand (via temperature) on GPP (*14-16*). Comparing θ_{crit} values diagnosed from the covariance of GPP and VPD (the 'VPD–GPP–SM method') with those calculated from EF–SM relationships (the 'EF–SM method') can help us understand whether evapotranspiration and photosynthetic processes become water-limited at similar SM conditions.

The relationship between EF and SM shows two regimes: energy-limited and water-limited evapotranspiration (*2, 5, 11, 12*). When SM is higher than θ_{crit}, the system is energy limited,

as less SM does not necessarily lead to lower evapotranspiration (*17, 18*). Evapotranspiration is at or near its potential value when net radiation is limiting, and EF stays near a maximum value (EF_{max}). In contrast, when SM is lower than θ_{crit}, the capacity of plants to extract soil water by roots and xylem transport becomes progressively reduced. Under this SM-limited regime, evapotranspiration decreases with decreasing SM until the wilting point, where transpiration is blocked because of full stomatal closure, with little or no further change in EF with SM decrease (*8*). In the SM-limited regime, EF decreases with decreasing SM, and this decrease is approximately linear (*8, 12, 19*). The soil moisture regime can self-amplify itself because a lower evapotranspiration increases surface temperature and VPD, and prevents the formation of boundary layer clouds (*3, 20*). These feedbacks further increase net radiation and atmospheric dryness at larger scales, which accelerates the depletion of soil moisture, causing a positive "dry gets dryer" land-atmosphere climate feedback (*4, 5, 21*).

The relationship between EF and SM can thus be summarized by three parameters: a constant EF_{max} in the energy limited regime, the θ_{crit} breaking point at which EF decreases with SM, and the linear slope (S) between EF and SM below this breaking point. This EF–SM framework is conceptually well established but quantifying θ_{crit} to delineate the transition from energy to water-limited regimes across biomes and climate zones has been mainly limited to model-based studies due to a lack of observations (*11, 18, 22, 23*). At the global scale, so far there is no observation-based assessment of θ_{crit}, S and EF_{max}, although few studies reported some of them at sites or regional scales (*13, 18, 22*). Even less is known about the mechanisms that control the three parameters of the EF–SM relationship. Earth system models include parametric functional SM–evaporation relationships, with parameters set to *ad hoc* values and kept constant in space and time (*24*). Differences in parameter values and functional relationships across models is a key source of divergence and uncertainty in their water and carbon cycle projections (*6, 18, 25*). Dirmeyer *et al*. (*25*) reported that an ensemble of models had no consistent representation of the connection between EF and SM. Quantifying the parameters of θ_{crit}, S and EF_{max} and their drivers across biomes and climates is therefore critical to identify the mechanisms of water stress tipping points and improve models to predict future climate accurately.

To quantify θ_{crit} directly, we used accurate and high-frequency measurements of EF from eddy covariance flux towers during extensive periods without rainfall, when a transition from energy to water limitation is likely to happen. These periods during when SM decreases are known as dry-downs (*18, 26, 27*). From a systematic analysis of multiple dry-downs, we derive the EF–SM relationship and θ_{crit} using daily latent and sensible heat flux observations from each site of the global network of flux tower measurements (Methods). The objectives of this study are (1) to quantify the three parameters θ_{crit}, S and EF_{max} of the EF–SM relationship across diverse plant functional groups and climate types; (2) to examine the climatic, biotic and edaphic predictors that control the spatial variability of θ_{crit}, S and EF_{max}; and (3) to investigate the consistency of θ_{crit} derived from the EF–SM and VPD–GPP–SM methods globally to determine whether evapotranspiration and photosynthetic processes become water-limited under similar soil moisture conditions. Based on these results, we then evaluate possible relationships between the parameters and test whether the observed varying responses of EF–SM can be explained by an optimality principle.

Results

Consistency of θ_{crit} derived from the EF–SM and VPD–GPP–SM methods

During a dry-down, EF remains relatively steady at first (energy-limited evapotranspiration stage) but then decreases when surface SM (volumetric soil water content, Methods) becomes lower than a given threshold. Fig. 1A shows this behavior at a forest site in Germany, DE-Hzd (Table S1). The EF–SM relationship is characterized by the θ_{crit} transition point in SM separating the water and energy-limited regimes. Using eight dry-downs recorded during two peak growing seasons, we find that surface θ_{crit} for EF equals 23.4 ± 0.5 % at this site (Fig. 1B). From the change in sign of the covariance between daily VPD and GPP (Fig. 1C), we find that surface θ_{crit} for GPP has a value of 24.5 %, which is very close to the EF-based estimate. Thus, θ_{crit} estimated for EF and GPP at this site are very similar.

Next, we systematically compared the two θ_{crit} values estimated from EF and GPP. Across all sites, the two methods give consistent results (r=0.82, Fig. 1D), suggesting that EF and GPP both become water-limited at similar SM conditions. Thus, the EF-SM relationship during dry-downs is an effective method to quantify the SM threshold of plant water stress, despite the fact that EF is also impacted by changes in bare soil evaporation, which is partly decoupled from the water stress on transpiration and GPP. A second point is that the VPD–GPP–SM method originally proposed for European ecosystems works globally, extending previous results from Fu, *et al*. (*13*). Since the VPD–GPP–SM method requires longer dry-down periods to calculate the covariance between daily VPD and GPP, the EF-SM method was retained for this study involving a large numbers of sites on a global scale (Fig. 1E). We systematically calculated the three parameters that fully explain the EF–SM relationship at each site, as shown in Fig. 1b, namely EF_{max} during the first part of the dry-downs in the absence of water stress, θ_{crit} for the inception of the EF decrease with SM, and the slope (S) of the linear relationship between EF and SM below θ_{crit}, when water stress intensifies.

θ_{crit}, S and EF_{max} among biomes and climate zones

We find that the θ_{crit} diagnosed from recurrent dry-downs of surface SM is highly correlated with the θ_{crit} estimated from deeper SM (Fig. S3). As surface SM measurements are available at all sites, we focus on surface SM. Across all sites globally, we find the median θ_{crit}, S and EF_{max} are 14.0 ± 0.9 % (± standard error), 0.045 ± 0.005 and 0.57 ± 0.02, respectively (Fig. S4). These three canonical parameters have notably large spatial variations, suggesting differences in behavior across biomes and climate zones (Fig. 2). The value of θ_{crit} in savannas (7.2 ± 1.1 %) is much lower than in deciduous broadleaf forests (DBF, 19.7 ± 2.4 %), grasslands (21.4 ± 2.4 %) and croplands (20.9 ± 2.5 %, Fig. 2A). Ecosystems in temperate (18.8 ± 1.3 %), continental (17.1 ± 3.3 %) and sub-tropical climates (14.7 ± 1.7 %) have higher θ_{crit} values than in dry climates (7.0 ± 1.1 %, Fig. 2B). The slope (S) value in savannas (0.082 ± 0.019) is three times higher than in grasslands (0.026 ± 0.009, Fig. 2C). Sites in temperate climates (0.033 ± 0.005) have lower S values than dry climates (0.090 ± 0.025, Fig. 2D). Regarding EF_{max}, the high values are mainly in croplands (0.78 ± 0.04), grasslands (0.67 ± 0.02) and DBF (0.63 ± 0.02), and they are significantly larger than in evergreen needleleaf forests (0.45 ± 0.02, Fig. 2E). Boreal climates (0.43 ± 0.04) have smaller EF_{max} values than tropical climates (0.71 ± 0.03, Fig. 2F). Combining biomes and climate types, the values of θ_{crit}, S and EF_{max} also varies among different ecosystems (Fig. S5), although statistical testing of these differences is impractical because of the limited sample size in each bin. We also find that variations of

the three parameters θ_{crit}, S and EF_{max} are substantial within any one biome or climate zone (Fig. 2), implying the existence of other local controlling factors.

Drivers of the spatial variability of θ_{crit}, S and EF_{max}

We analyse the relative importance of soil texture (sand fraction), vegetation structural characteristics (approximated by LAI_{max}) and mean climatic variables (mean VPD and total precipitation during peak growing season) on the spatial variability of θ_{crit}, S and EF_{max} using random forests (Methods). The cross-validation shows that these predictors explain 43%, 46% and 38% of the spatial variability of θ_{crit}, S and EF_{max}, respectively. The dominant predictors of the spatial variability of θ_{crit}, S and EF_{max} were however different. We find that the spatial variability of θ_{crit} is mostly explained by the sand fraction and LAI_{max} (Fig. 3A) while the spatial variability of S is mainly explained by VPD and LAI_{max} (Fig. 3F). The spatial variability of EF_{max} is mostly explained by precipitation amount, followed by LAI_{max} (Fig. 3K). Partial dependence analysis confirms that θ_{crit} across sites is reduced considerably with a higher sand fraction (Fig. 3B) but increased with LAI_{max} (Fig. 3C). In addition, θ_{crit} shows a positive dependence on precipitation (Fig. 3D) and a negative dependence on VPD (Fig. 3E). In contrast, S increases greatly with higher VPD (Fig. 3J), but decreases with increasing LAI_{max} (Fig. 3H). S is also less steep at higher precipitation (Fig. 3I) and for soils with a lower sand fraction (Fig. 3G). The opposite responses of θ_{crit} and S to all these four environmental factors (Figs. 3B-E, G-J) indicate that there is a negative relationship between θ_{crit} and S (see later). For EF_{max}, we find that increasing precipitation and LAI_{max} mainly enhance EF_{max} (Figs. 3M-N) while EF_{max} decreases with increasing sand fraction (Fig. 3L).

Relationships between θ_{crit}, S and EF_{max} and the optimal adaptation of local EF–SM responses

Across all sites, we find that θ_{crit} exhibits a significant negative correlation with S and a positive correlation with EF_{max} (Fig. 4A). This is further confirmed by partial correlation analysis (Fig. 4B). Thus, there is a trade-off between θ_{crit} and S: sites with low θ_{crit} often have high S values while sites with high θ_{crit} often have low S values (Fig. 4A, B). To understand the negative relationship between θ_{crit} and S, we define the intersection of the fitted segmented curve with the x-axis at each site as θ_0 (Methods). Across sites, the value of θ_0 do not significantly differ from zero (Fig. S7). The S values in different biomes can therefore be predicted using the ratio of EF_{max} and θ_{crit} (Fig. S8). The relationships between θ_{crit}, S and EF_{max} can be related to the dryness of the climate. We thus calculated the aridity index (AI), defined as the ratio of annual potential evapotranspiration to annual precipitation, from the eddy-covariance measurements at each site (Methods). We find that low θ_{crit} and high S values are more common in dry sites (AI > 4) while high θ_{crit} and low S values are more common in wet sites (AI<3, Fig. S9).

The distribution of θ_{crit} and S across different biomes leads us to hypothesize two strategies for how ecosystem have adapted to prevailing recurrent water stress: (1) low θ_{crit} with high S (e.g., savannas), and (2) high θ_{crit} with low S (e.g., grasslands (mainly in temperate and continental climates), Figs. 3A, 2A, C). The first strategy reflects a resistance to soil dryness and is more successful for ecosystems experiencing frequent dry-downs. However, below the infrequently reached θ_{crit} value, transpiration and ecosystem function may collapse rapidly. The second strategy, which consists in having a high EF_{max} and a high θ_{crit}, is better adapted to humid and sub-humid environments where dry-downs are shorter,

less severe and less frequent, so that the number of days with SM below θ_{crit} is low, and ecosystems can maximize EF_{max} to sustain water use for photosynthesis.

As both θ_{crit} and S values are significantly different between savannas and grasslands (Figs. 2A, C), the response functions of EF–SM in these two biomes are further compared (Methods). We find that the response curve of mean EF–SM in savannas and grasslands are in line with the general results observed across sites; namely θ_{crit} is negatively related to S but positively related to EF_{max} (Figs. 4A-C). The higher S value found in savannas implies that canopy conductance (G_c) may be reduced more strongly when SM passes below θ_{crit}, while the lower S value in grasslands indicates that G_c may decrease more progressively when SM unfrequently gets below θ_{crit}. To test this hypothesis, we calculated the reduction rate of G_c with decreasing SM under the water-limited stage in these two biomes, respectively (Methods). We find that the reduction rate of G_c with SM in savannas (9 ± 2 cm s^{-1} m^3 m^{-3}) is indeed significantly larger than in grasslands (5 ± 1 cm s^{-1} m^3 m^{-3}, Fig. 4D). Thus, the higher S values in savannas correspond to a stronger stomatal closure in response to a SM decrease under water-limited conditions, in order to prevent hydraulic failure. In contrast, the lower S values in grasslands imply a more gradual stomatal closure in response to SM decrease, favoring photosynthesis in periods of low to moderate water stress.

We formulated a second hypothesis that the contrasted response functions of EF–SM between savannas (low θ_{crit} and high S) and grasslands (high θ_{crit} and low S) locally maximize growing-season evapotranspiration and EF. To test this, we predicted the mean daily EF during the peak growing season for each site in savannas and grasslands by exchanging the two responses of EF–SM (from savannas to grasslands, and vice versa) (Methods). Comparing with observed and predicted mean daily EF using the true EF–SM response, we find that the predicted mean daily EF using the EF–SM response curve from the other biome is underestimated (Fig. 4E). This finding suggests that EF–SM response curves are adapted so as to maximize growing season EF. To further test whether maximizing EF also implies maximization of photosynthesis during the peak growing season, we performed the same analysis for GPP (Methods). We find that, in both savannas and grasslands, the predicted mean growing-season GPP using the EF–SM model of the other biome is always lower than the predicted GPP using the true EF–SM model (Fig. 4F). Thus, our results show that the trade-off between θ_{crit} and S helps to maximize the growing-season EF, and the optimal adaptation of the local EF–SM response function of the ecosystem can maximize growing-season evapotranspiration and photosynthesis. Except for savannas and grasslands, we could not compare the response functions of EF–SM among other biomes (forests, shrublands, croplands) because they do not have significant differences in either θ_{crit} or S (Figs. 2A, C).

Discussion

Vegetation regulates the terrestrial water and carbon cycles, as it controls and adapts to changing SM availability. Yet our ability to characterize the θ_{crit} at the global scale is limited. By examining the consistency of θ_{crit} estimated from the VPD–GPP–SM and EF–SM methods, this study showed that plant photosynthetic processes become water-stressed at a SM threshold similar to that of EF, suggesting that the EF–SM relationship is able to quantify the SM threshold of plant water stress. We noted that the absolute magnitudes of θ_{crit} values estimated from the VPD–GPP–SM method are slightly higher than those based on the EF–SM method (Fig. 1D). This higher value is likely due to the fact that the VPD–

GPP covariance is calculated using a nine-day moving window which therefore can overestimate the threshold during drydowns (*13*). Meanwhile, this bias may be also related to the bias in GPP for different flux tower sites due to the inhibition of leaf respiration in the light (*28*) and uncertainty in the gap-filling routine. The uncertainty in tower-estimated GPP depends in part on radiation, which would affect the SM thresholds estimated from VPD–GPP–SM method for different sites. Nevertheless, the relatively small mean difference, but strong spatial correlation between the two thresholds across all sites and all biomes shows that SM-limitation occurs at a similar SM level for GPP and evapotranspiration. This EF–SM approach used here also provided a practical application of the original conceptual Budyko curve (*11*), yet based on a temporal approach rather than spatial approach. The Budyko framework is commonly used to estimate the long-term mean actual evaporation as a function of the mean aridity index at the catchment scale and applied as a spatial analysis for mean evapotranspiration/precipitation (*29*). We focused here on the transient shift between energy and water limitations at the site scale (and at short time scales) and used SM to quantify ecosystem water limitation.

Land-surface models typically represent soil moisture stress effects on evapotranspiration and GPP as a segmented function (*30*), consistent with our empirical analysis. Some models set θ_{crit} at field capacity; then at lower SM, evapotranspiration and GPP are multiplied by a moisture scalar, which declines either linearly or non-linearly from 1 at field capacity to 0 at wilting point (*30*). Our results suggest that a linear formula with θ_{crit} set to field capacity will overestimate water stress. Other models more realistically define a θ_{crit} that is less than field capacity and greater than the wilting point (*31*). Additionally, a moisture scalar is also used in some satellite GPP and evapotranspiration algorithms. For example, satellite-driven light use efficiency (LUE) GPP models used environmental scalars to represent biophysical constraints on maximum LUE (*32, 33*), but many of the existing and widely used LUE models do not currently incorporate SM constraints directly (*34*). Our study provides a soil moisture stress framework and parameterization that could be incorporated in the future to improve these models. The formulation introduced in this study is also compatible with formulations already used in light-use efficiency and process-based land surface models, but the three parameter values here are based on analysis of measured data, providing observations of key parameters of the SM control on evapotranspiration. The θ_{crit} value we found is in line with the value found in Netherlands (16%) (*35*) and Africa (14%) (*18*) using satellite observations while our estimates of S and EF_{max} across sites are slightly higher than the values reported in Europe (S=0.03, EF_{max}=0.54) (*13*). We also found that there are large and systematic differences in these three parameters across biomes and climate zones. Even within a given plant functional type or climate type, the spatial variations in θ_{crit}, S and EF_{max} are also large. Thus, it is unrealistic to parameterize these variables as universal constants, like in many models. Although models simulate SM in different layers whereas our analysis was based on surface observations, our results demonstrate that the surface θ_{crit} is highly correlated with the θ_{crit} in deep soil layers (Fig. S3), which is consistent with the recent findings that surface and rootzone soil moisture are equivalently skillful for identifying evapotranspiration regime changes (*36*). We also found that, when surface θ_{crit} is larger than 20%, θ_{crit} based on SM dry-downs of the deep soil layers is higher than surface θ_{crit} (Fig. S3). This may be because the deep SM is relatively stable and acts as a low pass filter so that it will not be depleted as efficiently by plant roots compared with surface SM.

In addition to helping improve the representation of water stress in models, eddy covariance observations from globally distributed and automated sensor networks analysed

here with a machine learning approach also unravel new relationships between parameter values and environmental variables. Our results showed that the spatial variability of θ_{crit}, S, and EF_{max} are mostly explained by soil texture, mean growing season VPD and precipitation, respectively, while LAI_{max} also importantly affects their values. The variability of θ_{crit} is dominantly explained by the sand fraction, consistent with lower wilting points observed in sandy soils (*37*). Plant water stress is related to water potential which largely is impacted by the soil capacity to hold water (*38, 39*). Sandy soils have greater hydraulic conductivity and lower porosity than other soil types (e.g., clay) (*40, 41*), thus there is a lower soil water holding capacity in sandy soils. The spatial variability of S is mainly explained by VPD while the spatial variability of EF_{max} is mostly explained by the precipitation amount. Increasing VPD triggers stomatal closure (*14*) and reduces transpiration and EF, thus increasing S. LAI_{max} has important contributions to the spatial variability of all these three parameters, highlighting the critical role of vegetation structure in controlling evapotranspiration processes. This result is in keeping with a previous study from Williams and Torn (*42*), showing that LAI controls surface heat flux partitioning and land-atmosphere coupling. As they have a lower LAI_{max} and grow on more sandy soils (Fig. S10), savannas have lower θ_{crit} and higher S than that of grasslands. Grasslands also tend to have greater soil organic carbon, helping to increase the water holding capacity (*43*). Our results also showed that the θ_{crit} and S have opposite responses to all these environmental factors (soil texture, LAI_{max}, VPD and precipitation, Figs. 3B-E, G-J). We noted that these environmental factors only explained about 40% of the variance in θ_{crit}, S, and EF_{max}. The portion of unexplained variance might be related to plant hydraulic or functional traits, such as rooting depth or ability of roots to switch from surface to deep water uptake (*44-47*) and hydraulic traits diversity (*48*). Diverse communities are more likely to contain species with different traits that regulate how they respond to drought; higher hydraulic diversity for example buffers variation in ecosystem fluxes during dry periods across temperate and boreal forests (*48*). Given the large variations of these parameters over diverse ecosystems and the limited observational data we could use, we provide here a comprehensive analysis across global sites.

Our study sheds new light on varying EF–SM relationships in different ecosystems. Dryland ecosystems, such as savannas, operate at low θ_{crit}. Across sites, there is a negative relationship between θ_{crit} and S, indicating that dryland ecosystems, which minimize θ_{crit} through mechanisms of sustained soil water extraction and plant hydraulic transport, are also more vulnerable once extreme stress below θ_{crit} is reached. There is therefore a trade-off between θ_{crit} and S: sites with low θ_{crit} values often have high S values while sites with high θ_{crit} values often have low S values, indicating two different adaptation strategies. The first strategy reflects a resistance to soil dryness and is more successful for ecosystems experiencing frequent dry-downs. However, below the infrequently reached θ_{crit} value, ecosystem function may collapse rapidly. The second strategy with a high θ_{crit} is more adapted to humid and sub-humid environments where dry-downs are shorter and less severe. For the first strategy, the higher S values correspond to a more rapid stomatal closure in response to a SM decrease under water-limited conditions in order to prevent hydraulic failure (*49, 50*). In contrast, for the second strategy, the lower S values which is related to a more gradual stomatal closure in response to a SM decrease, benefits photosynthesis in periods of limited water stress and reduces the risk of carbon-starvation, but this can lead to hydraulic failure if drought is sufficiently intense: plants will run out of water before they run out of carbon (*51*).

The θ_{crit} values quantified in this study reflect a background ecosystem resistance to aridity. Berdugo *et al*. (*52*) recently reported that aridification is associated to systemic and abrupt changes, which occurred sequentially in three phases characterized by abrupt decays in plant productivity, soil fertility, and plant cover and richness at aridity values of 0.54, 0.7, and 0.8, respectively. Our results imply that ecosystems with lower θ_{crit} should have higher aridity thresholds. We do not have a map of θ_{crit} but with advances in remote sensing, this may be possible (e.g. Feldman *et al*. (*18*)) and we could then test if systems with a higher θ_{crit} have a lower threshold response to increased aridity compared to more resistant systems with a lower θ_{crit}. Consistent with the ecosystem optimality concepts, our results showed that the trade-off between θ_{crit} and S helps to increase the growing-season EF, and that optimal adaptation of the EF–SM response also maximizes growing-season carbon uptake. It is worth noting that different rooting depths across different sites may affect the θ_{crit}, although recent studies showed that surface and rootzone soil moisture are equivalently skillful for identifying evapotranspiration regime changes (*36*). We also noted that some species could utilize adaptation strategies to reduce LAI (e.g., drought deciduous functional types) in addition to stomatal regulation during dry periods (*53, 54*), but our analysis focused on peak growing season and soil dry-downs at short time scales, thus the impacts of drought deciduousness should be muted. Moreover, our analysis of the temporal dynamics of θ_{crit} showed that the interannual variability of θ_{crit} is not significant (Fig. S6), indicating the relatively stability of θ_{crit} through time in this study.

In summary, this study quantified the θ_{crit}, S, and EF_{max} in terrestrial ecosystems using globally-distributed eddy covariance measurement sites. Our formulation is similar to one commonly used in land surface models, although models consider deeper SM than observations. We found systematic differences of the three parameters across biomes and climates, and uncovered the relationships between parameter values and environmental factors, including climatic, biotic and edaphic variables. These results help in identifying tipping points of water stress impairing ecosystem functioning and should help towards a better representation of water stress in land surface models. Future research will aim to use our new understanding of θ_{crit}, S and EF_{max} to improve model representation of soil moisture constraints on water and carbon fluxes. As soil matric potential and VPD interact with vegetation function to control water flow, future research deriving relationships between SM during dry-downs, VPD, and soil water potentials will be a central challenge.

Materials and Methods

Eddy covariance observations

We used half-hourly soil moisture (SM), latent heat flux, sensible heat flux, vapor pressure deficit (VPD), gross primary productivity (GPP), and precipitation from the recently released ICOS (Integrated Carbon Observation System) (*55*), AmeriFlux (*56, 57*) and the FLUXNET2015 dataset of energy, water, and carbon fluxes and meteorological data, all of which have undergone a standardized set of quality control and gap filling (*58, 59*). Data were processed following a consistent and uniform processing pipeline (*58*). There are 279 flux tower sites in total by combing ICOS, AmeriFlux and FLUXNET2015 datasets. We first removed 62 sites without SM measurements, then dropped all wetland sites because they have a perched water table and infrequently show SM limitations such that 212 sites remained. Since for some sites, there was no dry-down detected during the peak growing season across all available years; these sites were also excluded (195 sites remaining). The

evaporative fraction (EF)–SM relationships in these 195 sites were evaluated to detect the θ_{crit} for each site.

SM was measured as volumetric soil water content (percentage) at different depths. Surface SM (SM_1: 0-10 cm, varying across sites) was measured at all sites and some sites also provided deeper SM measurements (e.g., SM_2: 10-30 cm; SM_3: 20-60 cm). We mainly explored the surface SM observations but deeper SM measurements were also used when available. The GPP estimates from the night-time partitioning method were used for the analysis (*60*). Data were quality controlled so that only measured and good-quality gap filled data (QC = 0 or 1) were used. Daytime half-hourly data (9 am to 16 pm local standard time) were averaged to daily values while SM values were averaged over the full day.

Soil moisture dry-down identification

Dry-downs following rainfall are episodes with no rain for several consecutive days during which SM shows a short term 'pulse' rise after rain and then decays until the next rain event. A dry-down is retained for our analysis when SM decreases consecutively for at least 10 days after rainfall following previous studies (*13, 26, 27, 61, 62*). Days with intermittent rainfall are excluded to remove the rainfall impacts on latent heat flux measurements. To minimize the irrigation effects on EF in croplands, we checked if there were peaks of SM without rain at each cropland site, which would indicate irrigation events. Then we removed the dry-downs with intense irrigation episodes at cropland sites. We focused on the soil dry-downs during the peak growing season for all available site-years, defined as 3-month period with the maximum mean GPP across the available years. This resulted in 2035 dry-down events that form the basis of our study.

θ_{crit}, S and EF_{max} estimation using EF–SM method

We calculated the daily EF as the ratio of observed latent heat flux to the sum of latent and sensible heat fluxes. Then, we characterized the EF–SM relationship at each site using all available soil dry-downs, from a regression between these two variables with a linear-plus-plateau model:

$$EF = \begin{cases} EF_{max} + S(SM - \theta_{crit}) & if\ SM < \theta_{crit} \\ EF_{max} & if\ SM \geq \theta_{crit} \end{cases} \quad (1)$$

where EF_{max} is the maximum value of EF in absence of SM stress (energy-limited stage), S represents the slope of the linear increase phase (water-limited stage), and θ_{crit} is the critical SM threshold. These three parameters and their standard errors were simultaneously estimated by least squares fit with the R software package 'segmented' (*63*) for each site, leading to site-specific estimated values of peak EF (EF_{max}), slope (S) and θ_{crit}. θ_{crit} is the breakpoint until which EF increases linearly as a function of SM. The S represents the EF sensitivity to SM in the water-limited regime, indicating the magnitude of EF increase for each additional 1 % soil water content (or 0.01 $m^3\ m^{-3}$) change in SM when SM is below its breakpoint. The plateau is the maximum EF value reached when SM exceeds its threshold. An example to estimate the EF_{max}, S and θ_{crit} was showed in Fig. 1B.

Based on the EF–SM relationships, there were 85, 29 and 19 sites with the θ_{crit} estimates using the first (SM_1), second (SM_2), and third (SM_3) soil water content measurement depth, respectively. For the rest of sites, it was not possible to estimate a θ_{crit} because

samples were too infrequent, or there were no thresholds. These 85 sites included 11 deciduous broadleaf forests (DBF), 5 evergreen broadleaf forests (EBF), 26 evergreen needleleaf forests (ENF), 3 mixed forests (MF), 8 shrublands (SHR), 4 croplands (CRO), 14 grasslands (GRA), and 14 savannas (SAV) (Table S1).

Differences in θ_{crit}, S and EF_{max} between groups (different plant functional types or climate types) were analyzed using the Kruskal–Wallis test, a nonparametric test of difference (*64*). A p-value <0.05 was used to identify significant differences between groups. Plant functional types were defined according to the International Geosphere–Biosphere Programme (IGBP) classification (*58*). Climate types were defined according to the Köppen-Geiger classification as in Migliavacca *et al*. (*65*): Tropical (Aw, Af, Am), Dry (BSh, BSk, BWh), Sub-Tropical (Cfa, Csa, Csb, Cwa), Temperate (Cfb), Continental (Dfa, Dfb, Dwa, Dwb, Dwc), and Boreal (Dfc, Dsc).

θ_{crit} estimation using VPD–GPP–SM method

For the threshold in plant photosynthetic processes, Fu *et al*. (*13*) recently reported that the initiation of water stress could be detected as the SM value when the sign of the covariance between daily GPP and VPD changes from positive to negative during a dry-down. GPP and evapotranspiration are tightly coupled on short time scales (*4*), and the sign of the covariance between daily VPD and GPP reflects the relative strength of water vs. energy limitation on ecosystem function, because VPD combines the effects of both water stress and energy demand (via temperature) on GPP (*14-16*). Following Fu *et al*. (*13*), we also calculated the covariance between daily VPD and GPP across nine-day moving windows during the dry-down (e.g., 1-9 days; 2-10 days; 3-11 days…). A positive covariance indicates that higher VPD is associated with increases of GPP (which we term 'radiation effects') while a negative covariance indicates that water stress limits GPP, i.e., with a higher VPD caused by dryer soils results in a lower GPP. We excluded some short dry-downs because their covariances during the dry-down are all positive or negative, suggesting the entire dry-down period is under energy-limited or water-limited stage. We only chose the long soil dry-downs with at least 15 days (with at least 7 covariance values) and their covariances must include both positive and negative values. Similar to the VPD–GPP covariance, the average of SM during the moving window (e.g., 1-9 days; 2-10 days; 3-11 days…) were also calculated to detect the θ_{crit} when the sign of VPD–GPP covariance changes from positive to negative. An example to quantify the θ_{crit} using VPD–GPP–SM method was showed in Fig. 1C.

To compare the θ_{crit} values from the VPD–GPP–SM method with the EF–SM method, we fitted the θ_{crit} values from these two methods using linear ($f(x) = p1 \times x + p2$) and nonlinear ($f(x) = p1 \times x^2 + p2 \times x + p3$) function, respectively (Fig. S1). We found that the coefficients of p1 and p2 in the linear fitting are significantly different from 0 at the significance level of 0.05 while both the p1 and p3 in the nonlinear fitting do not significantly differ from 0 (Fig. S1), suggesting that the linear assumption is reasonable. To test whether the closure of the energy balance from eddy covariance measurements affects the bias of θ_{crit} values (*66*), we repeated the analysis using the 'LE.CORR' and 'H.CORR' variables from FLUXNET database to calculate the EF and quantify θ_{crit}, instead of 'LE' and 'H'. LE.CORR and H.CORR are the "energy balance corrected" version of latent and sensible heat flux, based on the assumption that the Bowen ratio is correct (*67*). Our results were robust to either variable (Fig. S2). The differences in SM threshold values based on the two energy fluxes were negligible (Fig. S2).

Drivers of the spatial variability of θ_{crit}, S and EF_{max}

A random forests analysis was used to identify the soil property, vegetation structure and climate variables that contribute the most to the spatial variability of θ_{crit}, S and EF_{max}. For climatic variables, we calculated the aridity index, mean VPD, incoming shortwave radiation, wind speed and total precipitation during the peak growing season from flux tower observations at each site. As vegetation structure variable, maximum leaf area index (LAI_{max}) was collected for 53 sites, from the literature (*65, 68, 69*). Using the Application for Extracting and Exploring Analysis Ready Samples (AppEEARS) (*70*), LAI_{max} in the rest of 32 sites were extracted from MODIS LAI product (MCD15A2) at 500 m spatial resolution (*71*). Soil property variables were extracted from SoilGrids, a collections of soil property maps for the world at 250 m resolution (*72*), inculding sand fraction, soil organic carbon content, total nitrogen, pH, bulk density, volumetric fraction of coarse fragments and cation exchange capacity.

The performances of random forests model were assessed by 5-fold cross-validation using two criteria: the mean absolute error (MAE) and the R-squared value (R^2). MAE quantifies the overall error, while R^2 estimates the proportion of variance in response variable that is captured by the predictive variables. We favored the model with the smallest MAE and the highest R^2 (*73, 74*). Following Huang *et al*. (*73*), we first run the random forests model with all predictor variables included, then sequentially excluded predictors that did not improve model performance one after another. The best model with the minimum number of predictors and same predictors for all three response variables (θ_{crit}, S and EF_{max}) was selected. The final set of predictors included the following predictor variables: as soil property variable, sand fraction (%); as vegetation structure variable, maximum leaf area index (LAI_{max}, $m^2\ m^{-2}$); as climatic variables, mean daily VPD (hPa) and total precipitation amount (Preci, mm) during the peak growing season.

We used partial dependencies of variables to assess the relationship between individual predictors and the response variables (that is, $\theta_{crit,}$ S or EF_{max}). The results from the partial dependency analysis can be used to determine the effects of individual variables on the response, without the influence of the other variables (*74*). The partial dependencies were calculated restricted to the values falling within the convex hull of their training values to reduce the risk of interpreting the partial dependence plot outside the range of the data (extrapolation risk)(*65*). The partial dependence function was computed using the pdp R package (*75*). Partial dependence plots derived for θ_{crit}, S and EF_{max} were showed in Figs. 3B-E, G-J, L-O for various inputs.

Temporal variability of θ_{crit}, S and EF_{max}

Besides their spatial variability across sites, θ_{crit}, S and EF_{max} may also change with time. Although the temporal variability in θ_{crit}, S and EF_{max} is difficult to evaluate given the relatively short observation record at most sites, we analyzed the temporal dynamics of these three parameters at a forest site with long observational periods (2000-2019), DE-Hai (Table S1). We quantified θ_{crit}, S and EF_{max} using dry-downs every three years, respectively (Table S2, Note that we could not estimate a θ_{crit} during 2009-2017 because samples were too infrequent, or soil moisture was always above or below the threshold in these years). We found that θ_{crit} values changed slightly over time (Table S2). The mean θ_{crit}, S and EF_{max} across results from every three years were similar to that of during 2000-2019, thus our results reflect the average of θ_{crit}, S and EF_{max} during the available

observational periods. To further test whether there was a trend change through time in θ_{crit}, S and EF_{max}, we performed the same analysis at five sites with at least 15 years of measurements. We found that there was no significant trend change with time in the three parameters over all site-years (Fig. S6). This initial exploration should be treated with caution given the relatively few sites and short observation record.

Relationships between θ_{crit}, S and EF_{max}

To understand the relationships between θ_{crit}, S and EF_{max}, we plotted these three variables in three dimensions across all sites, distributed in different biomes or aridity index. Aridity index was defined as the ratio of annual potential evapotranspiration (PET) to annual precipitation. We calculated the PET using the Priestley-Taylor equation following Novick *et al*. (*16*) for each site. The aridity index calculated using PET from Priestley–Taylor equation matched well with that of the Penman–Monteith equation. We also performed the partial correlation analysis to test the significance of the relationships between θ_{crit}, S and EF_{max} ($P < 0.05$).

To further explore the negative relationship between θ_{crit} and S, we define the intersection of the fitted segmented curve with the x-axis as θ_0 (the value of SM at which EF equals zero), thus θ_0 can be calcualted using the Eq. 2.

$$S = \frac{EF_{max}}{(\theta_{crit} - \theta_0)} \quad (2)$$

We then compared the θ_0 with zero using t-test across sites and found that the θ_0 do not significantly differ from zero (Fig. S7). The S values in different biomes can therefore be predicted using the ratio of EF_{max} and θ_{crit} (Fig. S8).

Mean response function of EF–SM in savannas and grasslands

Based on the distribution of θ_{crit} and S in different plant functional types, we proposed two schema: (1) low θ_{crit} with high S (e.g., savannas), and (2) high θ_{crit} with low S (e.g., grasslands). As both θ_{crit} and S were significantly different between savannas and grasslands (Figs. 2A, C) and the number of sites in savannas (n=14) and grasslands (n=14) were same, the response functions of EF–SM in these two biomes were further compared. We were not able to compare the response functions of EF–SM among other biomes becasuse they did not show any significant difference in either θ_{crit} or S (Figs. 2A, C). The mean response functions of EF–SM in savannas and grasslands were obtained by calculating the median values of the θ_{crit}, S and EF_{max} across all sites for savannas and grasslands, respectively. The uncertainty of mean EF–SM response function for each biome was quantified by calculating the 95% confidence interval across all sites.

Derivation of canopy conductance from eddy covariance measurements

At each site in savannas and grasslands, G_c under water-limited stage (SM < θ_{crit}) was calculated using half-hourly eddy-covariance measurements by inverting the Penman–Monteith equation (*76*):

$$G_c = r_a\gamma / \left(\frac{\Delta(R_n - G) + \rho c_p r_a (e_s(T_a) - e_a)}{\lambda E} - (\Delta + \lambda) \right) \quad (3)$$

where G_c and r_a are canopy stomatal conductance and aerodynamic resistance respectively, γ is the psychrometric constant, Δ is the slope of the water vapour deficit with respect to temperature, R_n and G are observed net radiation and soil heat flux, ρ is air density, C_p is the specific heat capacity of dry air, e_s and e_a are saturated and actual vapor pressure, and λE is observed evapotranspiration. r_a is calculated following Novick *et al*. (*16*) (Eq. 4), using the von Kármán constant ($k = 0.4$), available wind speed data (w_s), measurement height (z_m), momentum roughness length ($z_0 = 0.1h$) and zero plane displacement ($z_d = 0.67h$), both based on calculated canopy height (h) under near-neutral conditions (*77*) (Eq. 5).

$$r_a = \frac{\ln\left(\frac{z_m - z_d}{z_0}\right)^2}{w_s k^2} \quad (4)$$

$$h = \frac{z_m}{0.6 + 0.1 \times exp\left(\frac{k w_s}{u^*}\right)} \quad (5)$$

In order to evaluate the reduction rate of G_c per SM decrease under water-limited stage, we further calculated the change rate of G_c under water-limited stage for each site in savannas and grasslands by the ratio between the change of G_c and the change of SM as follows (Eq. 6):

$$\Delta G_c = \frac{Median(G_{SM\ in\ 80-100th}) - Median(G_{SM\ in\ 0-20th})}{Median(SM_{80-100th}) - Median(SM_{0-20th})} \quad (6)$$

where ΔG_c is the reduction rate of G_c per SM decrease; $Median(G_{SM\ in\ 80-100th})$ is the median G_c during 80-100th percentiles of SM under water-limited stage; $Median(G_{SM\ in\ 0-20th})$ is the median G_c during 0-20th percentiles of SM under water-limited stage; $Median(SM_{80-100th})$ is the median SM during 80-100th percentiles of SM under water-limited stage, and $Median(SM_{0-20th})$ is the median SM during 0-20th percentiles of SM under water-limited stage.

Predicting EF and GPP during the peak growing season

We formulated the hypothesis that, the distinct response functions of EF–SM between savannas (low θ_{crit} with high S) and grasslands (high θ_{crit} with low S) locally maximize growing-season EF. To test this, we predicted mean daily EF during the peak growing season in savannas by swapping two response functions of EF–SM, the one from savannas and the one from grasslands. Similarly, we predicted mean daily EF during the peak growing season in grasslands for each site using daily SM in grasslands and running two response functions of EF–SM, respectively.

To further test whether the maximizing EF also reflect a production maximization during the peak growing season, we performed the same analysis for savannas and grasslands GPP using daily observed EF and predicted EF from two response functions of EF–SM, respectively. Mean daily GPP during the peak growing season for each site was calculated using daily EF, net radiation (R_n) and water use efficiency (WUE) as Eq. 7. WUE was calculated as the ration of observed GPP to observed latent heat flux (*78*). Except for savannas and grasslands, we cannot compare the response functions of EF–SM among other biomes because they have no significant difference in either θ_{crit} or S (Figs. 2A, C).

$$GPP = EF \times R_n \times WUE \quad (7)$$

References

1. M. Bassiouni, S. P. Good, C. J. Still, C. W. Higgins, Plant water uptake thresholds inferred from satellite soil moisture. *Geophysical Research Letters* **47**, e2020GL087077 (2020).
2. I. Rodriguez-Iturbe, Ecohydrology: A hydrologic perspective of climate-soil-vegetation dynamies. *Water Resources Research* **36**, 3-9 (2000).
3. P. Gentine, A. Chhang, A. Rigden, G. Salvucci, Evaporation estimates using weather station data and boundary layer theory. *Geophysical Research Letters* **43**, 11,661-611,670 (2016).
4. P. Gentine, J. K. Green, M. Guérin, V. Humphrey, S. I. Seneviratne, Y. Zhang, S. Zhou, Coupling between the terrestrial carbon and water cycles—a review. *Environmental Research Letters* **14**, 083003 (2019).
5. S. I. Seneviratne, T. Corti, E. L. Davin, M. Hirschi, E. B. Jaeger, I. Lehner, B. Orlowsky, A. J. Teuling, Investigating soil moisture–climate interactions in a changing climate: A review. *Earth-Science Reviews* **99**, 125-161 (2010).
6. C. Schwingshackl, M. Hirschi, S. I. Seneviratne, Quantifying spatiotemporal variations of soil moisture control on surface energy balance and near-surface air temperature. *Journal of Climate* **30**, 7105-7124 (2017).
7. I. Rodríguez-Iturbe, A. Porporato, *Ecohydrology of water-controlled ecosystems: soil moisture and plant dynamics* (Cambridge University Press, 2007).
8. F. Laio, A. Porporato, L. Ridolfi, I. Rodriguez-Iturbe, Plants in water-controlled ecosystems: active role in hydrologic processes and response to water stress: II. Probabilistic soil moisture dynamics. *Advances in water resources* **24**, 707-723 (2001).
9. J. A. Santanello Jr, P. A. Dirmeyer, C. R. Ferguson, K. L. Findell, A. B. Tawfik, A. Berg, M. Ek, P. Gentine, B. P. Guillod, C. Van Heerwaarden, Land–atmosphere interactions: The LoCo perspective. *Bulletin of the American Meteorological Society* **99**, 1253-1272 (2018).
10. P. Zhang, J.-H. Jeong, J.-H. Yoon, H. Kim, S.-Y. S. Wang, H. W. Linderholm, K. Fang, X. Wu, D. Chen, Abrupt shift to hotter and drier climate over inner East Asia beyond the tipping point. *Science* **370**, 1095-1099 (2020).
11. M. I. Budyko, *Climate and life* (Academic press, 1974).
12. P. S. Eagleson, Climate, soil, and vegetation: 4. The expected value of annual evapotranspiration. *Water Resources Research* **14**, 731-739 (1978).
13. Z. Fu, P. Ciais, D. Makowski, A. Bastos, P. C. Stoy, A. Ibrom, A. Knohl, M. Migliavacca, M. Cuntz, L. Sigut, M. Peichl, D. Loustau, T. S. El-Madany, N. Buchmann, M. Gharun, I. Janssens, C. Markwitz, T. Grunwald, C. Rebmann, M. Molder, A. Varlagin, I. Mammarella, P. Kolari, C. Bernhofer, M. Heliasz, C. Vincke, A. Pitacco, E. Cremonese, L. Foltynova, J. P. Wigneron, Uncovering the critical soil moisture thresholds of plant water stress for European ecosystems. *Glob Chang Biol*, (2021).
14. C. Grossiord, T. N. Buckley, L. A. Cernusak, K. A. Novick, B. Poulter, R. T. Siegwolf, J. S. Sperry, N. G. McDowell, Plant responses to rising vapor pressure deficit. *New Phytologist* **226**, 1550-1566 (2020).
15. H. Kimm, K. Guan, P. Gentine, J. Wu, C. J. Bernacchi, B. N. Sulman, T. J. Griffis, C. Lin, Redefining droughts for the U.S. Corn Belt: The dominant role of atmospheric vapor pressure deficit over soil moisture in regulating stomatal behavior of Maize and Soybean. *Agricultural and Forest Meteorology* **287**, 107930 (2020).
16. K. A. Novick, D. L. Ficklin, P. C. Stoy, C. A. Williams, G. Bohrer, A. C. Oishi, S. A. Papuga, P. D. Blanken, A. Noormets, B. N. Sulman, The increasing importance of atmospheric demand for ecosystem water and carbon fluxes. *Nature Climate Change* **6**, 1023 (2016).
17. A. G. Pendergrass, G. A. Meehl, R. Pulwarty, M. Hobbins, A. Hoell, A. AghaKouchak, C. J. Bonfils, A. J. Gallant, M. Hoerling, D. Hoffmann, Flash droughts present a new challenge for subseasonal-to-seasonal prediction. *Nature Climate Change* **10**, 191-199 (2020).

18. A. F. Feldman, D. J. Short Gianotti, I. F. Trigo, G. D. Salvucci, D. Entekhabi, Satellite-based assessment of land surface energy partitioning–soil moisture relationships and effects of confounding variables. *Water Resources Research* **55**, 10657-10677 (2019).

19. A. Porporato, P. D'odorico, F. Laio, L. Ridolfi, I. Rodriguez-Iturbe, Ecohydrology of water-controlled ecosystems. *Advances in Water Resources* **25**, 1335-1348 (2002).

20. S. I. Seneviratne, M. Wilhelm, T. Stanelle, B. van den Hurk, S. Hagemann, A. Berg, F. Cheruy, M. E. Higgins, A. Meier, V. Brovkin, Impact of soil moisture-climate feedbacks on CMIP5 projections: First results from the GLACE-CMIP5 experiment. *Geophysical Research Letters* **40**, 5212-5217 (2013).

21. A. K. Betts, Understanding hydrometeorology using global models. *Bulletin of the American Meteorological Society* **85**, 1673-1688 (2004).

22. D. D. Baldocchi, L. Xu, N. Kiang, How plant functional-type, weather, seasonal drought, and soil physical properties alter water and energy fluxes of an oak–grass savanna and an annual grassland. *Agricultural and Forest Meteorology* **123**, 13-39 (2004).

23. R. Koster, S. Schubert, M. Suarez, Analyzing the concurrence of meteorological droughts and warm periods, with implications for the determination of evaporative regime. *Journal of Climate* **22**, 3331-3341 (2009).

24. K. W. Oleson, D. M. Lawrence, B. Gordon, M. G. Flanner, E. Kluzek, J. Peter, S. Levis, S. C. Swenson, E. Thornton, J. Feddema, Technical description of version 4.0 of the Community Land Model (CLM). (2010).

25. P. A. Dirmeyer, R. D. Koster, Z. Guo, Do global models properly represent the feedback between land and atmosphere? *Journal of Hydrometeorology* **7**, 1177-1198 (2006).

26. R. Akbar, D. J. S. Gianotti, K. A. McColl, E. Haghighi, G. D. Salvucci, D. Entekhabi, Estimation of landscape soil water losses from satellite observations of soil moisture. *Journal of Hydrometeorology* **19**, 871-889 (2018).

27. A. F. Feldman, D. J. S. Gianotti, A. G. Konings, K. A. McColl, R. Akbar, G. D. Salvucci, D. Entekhabi, Moisture pulse-reserve in the soil-plant continuum observed across biomes. *Nature plants* **4**, 1026-1033 (2018).

28. T. F. Keenan, M. Migliavacca, D. Papale, D. Baldocchi, M. Reichstein, M. Torn, T. Wutzler, Widespread inhibition of daytime ecosystem respiration. *Nature Ecology & Evolution* **3**, 407-415 (2019).

29. A. Gerrits, H. Savenije, E. Veling, L. Pfister, Analytical derivation of the Budyko curve based on rainfall characteristics and a simple evaporation model. *Water Resources Research* **45**, (2009).

30. G. Bonan, *Climate change and terrestrial ecosystem modeling* (Cambridge University Press, 2019).

31. K. Van Looy, J. Bouma, M. Herbst, J. Koestel, B. Minasny, U. Mishra, C. Montzka, A. Nemes, Y. A. Pachepsky, J. Padarian, Pedotransfer functions in Earth system science: challenges and perspectives. *Reviews of Geophysics* **55**, 1199-1256 (2017).

32. W. Kolby Smith, S. C. Reed, C. C. Cleveland, A. P. Ballantyne, W. R. Anderegg, W. R. Wieder, Y. Y. Liu, S. W. Running, Large divergence of satellite and Earth system model estimates of global terrestrial CO2 fertilization. *Nature climate change* **6**, 306-310 (2016).

33. Y. Pei, J. Dong, Y. Zhang, W. Yuan, R. Doughty, J. Yang, D. Zhou, L. Zhang, X. Xiao, Evolution of light use efficiency models: Improvement, uncertainties, and implications. *Agricultural and Forest Meteorology* **317**, 108905 (2022).

34. B. D. Stocker, J. Zscheischler, T. F. Keenan, I. C. Prentice, S. I. Seneviratne, J. Peñuelas, Drought impacts on terrestrial primary production underestimated by satellite monitoring. *Nature Geoscience* **12**, 264-270 (2019).

35. J. Buitink, A. M. Swank, M. van der Ploeg, N. E. Smith, H.-J. F. Benninga, F. van der Bolt, C. D. Carranza, G. Koren, R. van der Velde, A. J. Teuling, Anatomy of the 2018 agricultural drought in the Netherlands using in situ soil moisture and satellite vegetation indices. *Hydrology and earth system sciences* **24**, 6021-6031 (2020).

36. J. Dong, R. Akbar, D. J. Short Gianotti, A. F. Feldman, W. T. Crow, D. Entekhabi, Can Surface Soil Moisture Information Identify Evapotranspiration Regime Transitions? *Geophysical Research Letters*, e2021GL097697 (2022).

37. G. Bonan, *Ecological climatology: concepts and applications* (Cambridge University Press, 2015).

38. Y. Shao, P. Irannejad, On the choice of soil hydraulic models in land-surface schemes. *Boundary-Layer Meteorology* **90**, 83-115 (1999).

39. K. A. Novick, D. L. Ficklin, D. Baldocchi, K. J. Davis, T. A. Ghezzehei, A. G. Konings, N. MacBean, N. Raoult, R. L. Scott, Y. Shi, B. N. Sulman, J. D. Wood, Confronting the water potential information gap. *Nat Geosci* **15**, 158-164 (2022).

40. M. T. Van Genuchten, A closed-form equation for predicting the hydraulic conductivity of unsaturated soils. *Soil science society of America journal* **44**, 892-898 (1980).

41. Y. Mualem, A new model for predicting the hydraulic conductivity of unsaturated porous media. *Water resources research* **12**, 513-522 (1976).

42. I. N. Williams, M. S. Torn, Vegetation controls on surface heat flux partitioning, and land-atmosphere coupling. *Geophysical Research Letters* **42**, 9416-9424 (2015).

43. W. Chen, P. Ciais, D. Zhu, A. Ducharne, N. Viovy, C. Qiu, C. Huang, Feedbacks of soil properties on vegetation during the Green Sahara period. *Quaternary Science Reviews* **240**, 106389 (2020).

44. Y. Liu, N. M. Holtzman, A. G. Konings, Global ecosystem-scale plant hydraulic traits retrieved using model–data fusion. *Hydrology and Earth System Sciences* **25**, 2399-2417 (2021).

45. J. Kattge, S. Diaz, S. Lavorel, I. C. Prentice, P. Leadley, G. Bönisch, E. Garnier, M. Westoby, P. B. Reich, I. J. Wright, TRY–a global database of plant traits. *Global change biology* **17**, 2905-2935 (2011).

46. Y. Fan, G. Miguez-Macho, E. G. Jobbágy, R. B. Jackson, C. Otero-Casal, Hydrologic regulation of plant rooting depth. *Proceedings of the National Academy of Sciences* **114**, 10572-10577 (2017).

47. Y. Yang, R. J. Donohue, T. R. McVicar, Global estimation of effective plant rooting depth: Implications for hydrological modeling. *Water Resources Research* **52**, 8260-8276 (2016).

48. W. R. Anderegg, A. G. Konings, A. T. Trugman, K. Yu, D. R. Bowling, R. Gabbitas, D. S. Karp, S. Pacala, J. S. Sperry, B. N. Sulman, Hydraulic diversity of forests regulates ecosystem resilience during drought. *Nature* **561**, 538-541 (2018).

49. A. G. Konings, P. Gentine, Global variations in ecosystem-scale isohydricity. *Global Change Biology* **23**, 891-905 (2017).

50. N. G. McDowell, Mechanisms linking drought, hydraulics, carbon metabolism, and vegetation mortality. *Plant physiology* **155**, 1051-1059 (2011).

51. N. McDowell, W. T. Pockman, C. D. Allen, D. D. Breshears, N. Cobb, T. Kolb, J. Plaut, J. Sperry, A. West, D. G. Williams, Mechanisms of plant survival and mortality during drought: why do some plants survive while others succumb to drought? *New phytologist* **178**, 719-739 (2008).

52. M. Berdugo, M. Delgado-Baquerizo, S. Soliveres, R. Hernández-Clemente, Y. Zhao, J. J. Gaitán, N. Gross, H. Saiz, V. Maire, A. Lehmann, Global ecosystem thresholds driven by aridity. *Science* **367**, 787-790 (2020).

53. W. K. Smith, M. P. Dannenberg, D. Yan, S. Herrmann, M. L. Barnes, G. A. Barron-Gafford, J. A. Biederman, S. Ferrenberg, A. M. Fox, A. Hudson, Remote sensing of dryland ecosystem structure and function: Progress, challenges, and opportunities. *Remote Sensing of Environment* **233**, 111401 (2019).

54. K. Dahlin, R. Fisher, P. Lawrence, Environmental drivers of drought deciduous phenology in the Community Land Model. *Biogeosciences* **12**, 5061-5074 (2015).

55. Warm Winter 2020 Team, & ICOS Ecosystem Thematic Centre. (2022). Warm Winter 2020 ecosystem eddy covariance flux product for 73 stations in FLUXNET-Archive format—release 2022-1 (Version 1.0). ICOS Carbon Portal. https://doi.org/10.18160/2G60-ZHAK

56. K. A. Novick, J. Biederman, A. Desai, M. Litvak, D. J. Moore, R. Scott, M. Torn, The AmeriFlux network: A coalition of the willing. *Agricultural and Forest Meteorology* **249**, 444-456 (2018).

57. X. Lu, T. F. Keenan, No evidence for a negative effect of growing season photosynthesis on leaf senescence timing. *Global Change Biology*.

58. G. Pastorello, C. Trotta, E. Canfora, H. Chu, D. Christianson, Y.-W. Cheah, C. Poindexter, J. Chen, A. Elbashandy, M. Humphrey, The FLUXNET2015 dataset and the ONEFlux processing pipeline for eddy covariance data. *Scientific data* **7**, 1-27 (2020).

59. D. Baldocchi, E. Falge, L. Gu, R. Olson, D. Hollinger, S. Running, P. Anthoni, C. Bernhofer, K. Davis, R. Evans, FLUXNET: a new tool to study the temporal and spatial variability of ecosystem-scale carbon dioxide, water vapor, and energy flux densities. *Bulletin of the American Meteorological Society* **82**, 2415-2434 (2001).

60. M. Reichstein, E. Falge, D. Baldocchi, D. Papale, M. Aubinet, P. Berbigier, C. Bernhofer, N. Buchmann, T. Gilmanov, A. Granier, On the separation of net ecosystem exchange into assimilation and ecosystem respiration: review and improved algorithm. *Global Change Biology* **11**, 1424-1439 (2005).

61. K. A. McColl, W. Wang, B. Peng, R. Akbar, D. J. Short Gianotti, H. Lu, M. Pan, D. Entekhabi, Global characterization of surface soil moisture drydowns. *Geophysical Research Letters* **44**, 3682-3690 (2017).

62. P. J. Shellito, E. E. Small, B. Livneh, Controls on surface soil drying rates observed by SMAP and simulated by the Noah land surface model. *Hydrology and Earth System Sciences* **22**, 1649-1663 (2018).

63. V. M. Muggeo, Segmented: an R package to fit regression models with broken-line relationships. *R news* **8**, 20-25 (2008).

64. P. E. McKight, J. Najab, Kruskal-wallis test. *The corsini encyclopedia of psychology*, 1-1 (2010).

65. M. Migliavacca, T. Musavi, M. D. Mahecha, J. A. Nelson, J. Knauer, D. D. Baldocchi, O. Perez-Priego, R. Christiansen, J. Peters, K. Anderson, The three major axes of terrestrial ecosystem function. *Nature* **598**, 468-472 (2021).

66. M. Jung, M. Reichstein, H. A. Margolis, A. Cescatti, A. D. Richardson, M. A. Arain, A. Arneth, C. Bernhofer, D. Bonal, J. Chen, Global patterns of land-atmosphere fluxes of carbon dioxide, latent heat, and sensible heat derived from eddy covariance, satellite, and meteorological observations. *Journal of Geophysical Research: Biogeosciences* **116**, (2011).

67. T. E. Twine, W. Kustas, J. Norman, D. Cook, P. Houser, T. Meyers, J. Prueger, P. Starks, M. Wesely, Correcting eddy-covariance flux underestimates over a grassland. *Agricultural and forest meteorology* **103**, 279-300 (2000).

68. M. Migliavacca, M. Reichstein, A. D. Richardson, R. Colombo, M. A. Sutton, G. Lasslop, E. Tomelleri, G. Wohlfahrt, N. Carvalhais, A. Cescatti, Semiempirical modeling of abiotic and biotic factors controlling ecosystem respiration across eddy covariance sites. *Global Change Biology* **17**, 390-409 (2011).

69. C. R. Flechard, A. Ibrom, U. M. Skiba, W. d. Vries, M. v. Oijen, D. R. Cameron, N. B. Dise, J. F. Korhonen, N. Buchmann, A. Legout, Carbon–nitrogen interactions in European forests and semi-natural vegetation–Part 1: Fluxes and budgets of carbon, nitrogen and greenhouse gases from ecosystem monitoring and modelling. *Biogeosciences* **17**, 1583-1620 (2020).

70. L. DAAC. (2021).

71. R. Myneni, Y. Knyazikhin, T. Park, MOD15A2H MODIS/terra leaf area index. *FPAR 8-day L4 Global 500 m SIN Grid V006 Data Set*, (2015).

72. L. Poggio, L. M. De Sousa, N. H. Batjes, G. Heuvelink, B. Kempen, E. Ribeiro, D. Rossiter, SoilGrids 2.0: producing soil information for the globe with quantified spatial uncertainty. *Soil* **7**, 217-240 (2021).

73. Y. Huang, P. Ciais, M. Santoro, D. Makowski, J. Chave, D. Schepaschenko, R. Z. Abramoff, D. S. Goll, H. Yang, Y. Chen, A global map of root biomass across the world's forests. *Earth System Science Data* **13**, 4263-4274 (2021).

74. J. K. Green, A. Ballantyne, R. Abramoff, P. Gentine, D. Makowski, P. Ciais, Surface temperatures reveal patterns of vegetation water stress and their environmental drivers across the tropical Americas. *Global Change Biology*, (2022).

75. J. H. Friedman, Greedy function approximation: a gradient boosting machine. *Annals of statistics*, 1189-1232 (2001).

76. J. Monteith, Evaporation and surface temperature. *Quarterly Journal of the Royal Meteorological Society* **107**, 1-27 (1981).

77. S. Pennypacker, D. Baldocchi, Seeing the fields and forests: Application of surface-layer theory and flux-tower data to calculating vegetation canopy height. *Boundary-layer meteorology* **158**, 165-182 (2016).

78. T. F. Keenan, D. Y. Hollinger, G. Bohrer, D. Dragoni, J. W. Munger, H. P. Schmid, A. D. Richardson, Increase in forest water-use efficiency as atmospheric carbon dioxide concentrations rise. *Nature* **499**, 324-327 (2013).

Acknowledgments

We would like to thank the ICOS Infrastructure for support in collecting and curating the eddy covariance data. This work used global eddy covariance data acquired and shared by the FLUXNET community, including these networks: AmeriFlux, AfriFlux, AsiaFlux, CarboAfrica, CarboEuropeIP, CarboItaly, CarboMont, ChinaFlux, Fluxnet-Canada, GreenGrass, ICOS, KoFlux, LBA, NECC, OzFlux-TERN, TCOS-Siberia and USCCC. The ERA-Interim reanalysis data are provided by ECMWF and processed by LSCE. The FLUXNET eddy covariance data processing and harmonization were carried out by the European Fluxes Database Cluster, AmeriFlux Management Project and Fluxdata project of FLUXNET, with the support of CDIAC and ICOS Ecosystem Thematic Center and the OzFlux, ChinaFlux and AsiaFlux offices.

Funding: This work was financially supported by the European Research Council Synergy project SyG-2013-610028 IMBALANCE-P and the ANR CLAND Convergence Institute. Z.F. acknowledges support from the CNES (5100019800). I.C.P. acknowledges support by European Research Council funding under the European Union's Horizon 2020 research and innovation programme (grant agreement No: 787203 REALM). I.C.P. and P.G. acknowledge support by the LEMONTREE (Land Ecosystem Models based On New Theory, observation and Experiments) project, funded through the generosity of Eric and Wendy Schmidt by recommendation of the Schmidt Futures programme.

Author contributions: P.C. and Z.F. designed the study. Z.F. performed the analysis. Z.F. and P.C. wrote the paper with the inputs from all co-authors. A.F.F., I.C.P., P.G., J.P.W, D.M., P.C.S., and A.B. provided methodological suggestions and contributed to the interpretation of the results.

Competing interests: The authors declare that they have no competing interests.

Data and materials availability: All data needed to evaluate the conclusions in the paper are present in the paper and/or the Supplementary Materials. The eddy covariance measurements are obtained from the ICOS (https://doi.org/10.18160/2G60-ZHAK), AmeriFlux (https://ameriflux.lbl.gov/) and FLUXNET2015 datasets (https://fluxnet.fluxdata.org/data/fluxnet2015-dataset/).

Figures

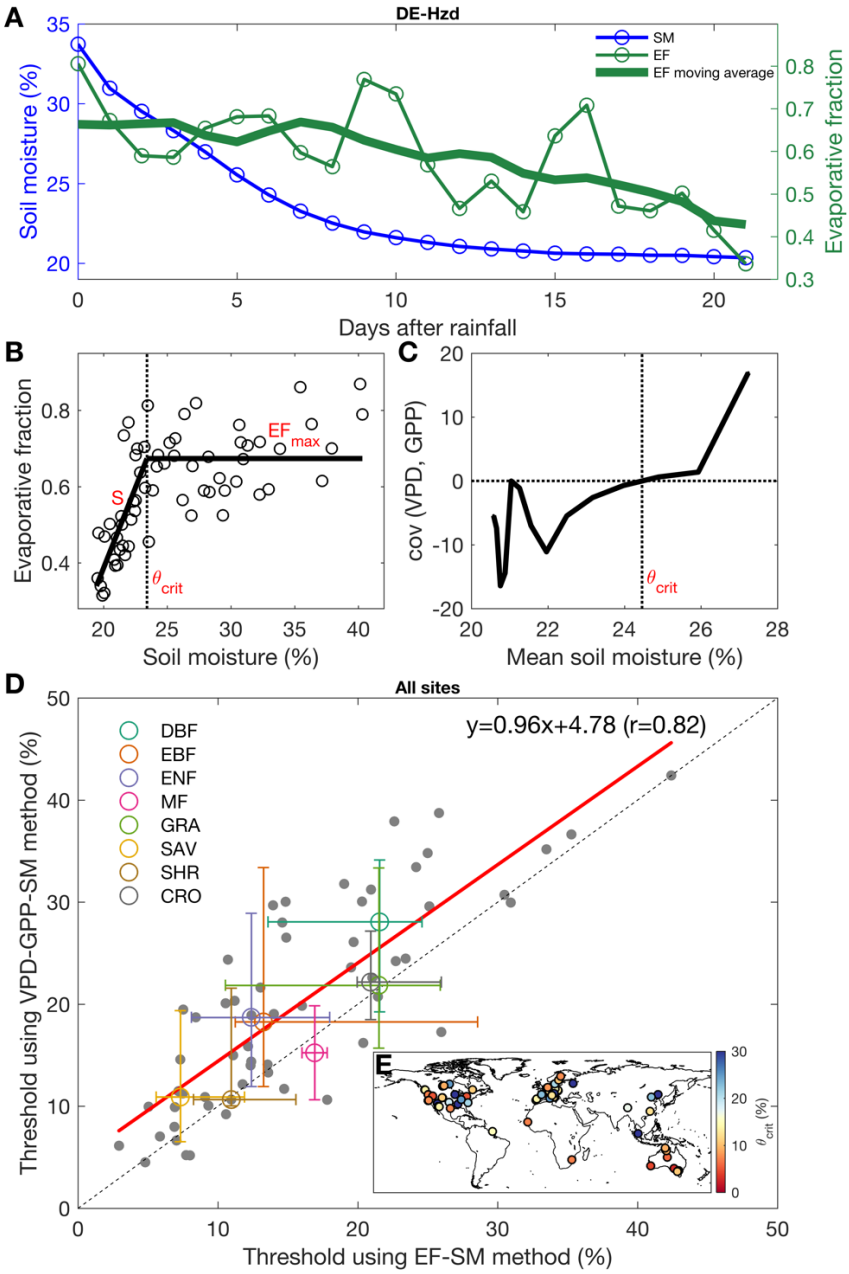

Fig. 1. Quantifying the critical SM threshold during SM dry-downs using EF–SM method and VPD–GPP–SM method. SM and EF changes during a dry-down at a forest site, DE-Hzd (A). Estimating SM threshold from the EF–SM method (B) and the VPD–GPP–SM method (C) using all dry-downs at DE-Hzd. Comparison between the SM thresholds estimated from the VPD–GPP–SM method and the EF–SM method across all sites (D). Median and the 25th, 75th percentiles are shown for each biome. The dashed line is the 1:1 line. Covariance and mean SM were calculated using 9-day moving window (e.g., 1-9 days; 2-10 days; 3-11 days…) following Fu *et al*. (*13*). The units of covariance between VPD and GPP is µmol CO_2 m^{-2} s^{-1} hPa. Map of the flux tower sites used in this analysis (E). Colours indicate the θ_{crit} values using EF–SM method. SM: soil moisture; EF: evaporative fraction; VPD: vapor pressure deficit; GPP: gross primary production; θ_{crit}: critical SM threshold; S: slope between EF and SM; EF_{max}: peak EF.

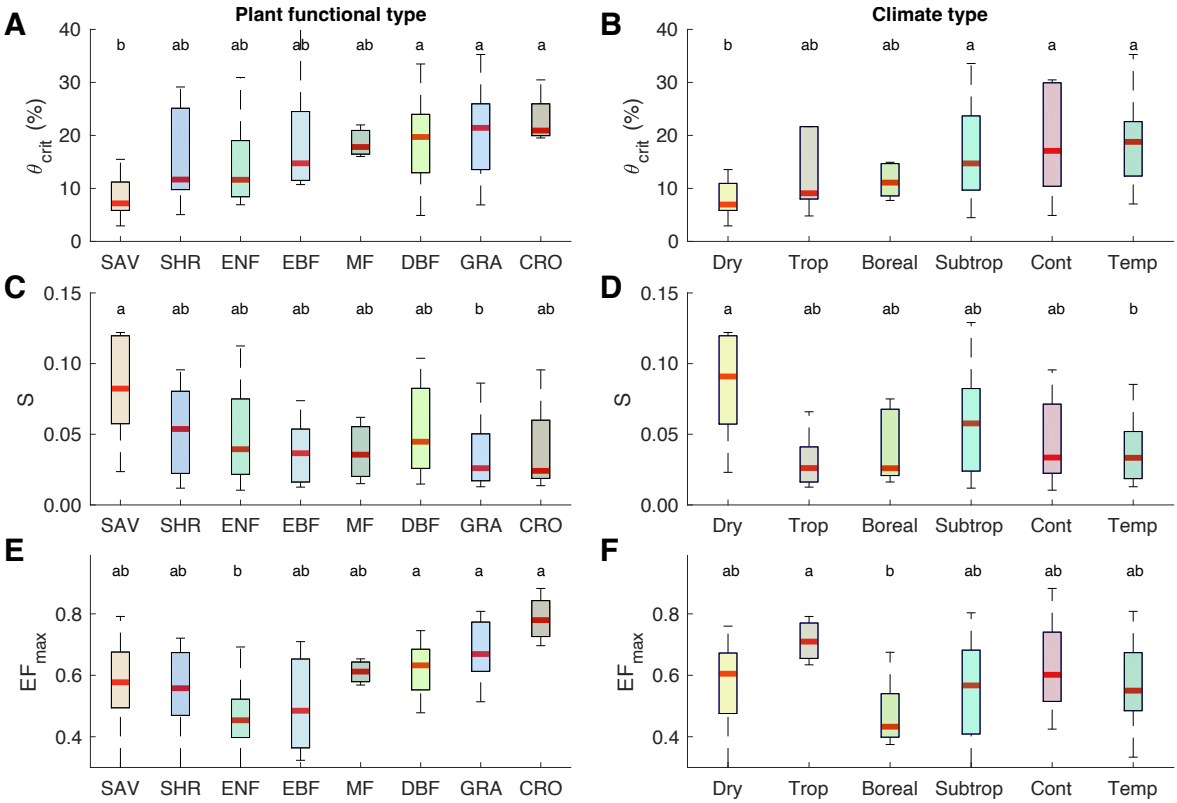

Fig. 2. Soil moisture threshold (θ_{crit}), evaporative fraction slope (S) and peak evaporative fraction (EF_{max}) among different plant functional types and climate types. θ_{crit} (A-B), S (C-D), and EF_{max} (E-F) among different plant functional types (A, C, E) and climate types (B, D, F). Letters represent statistically significant differences in the median values (Kruskal-Wallis test, $P < 0.05$), such that groups not containing the same letter are different. For each box plot, the middle line indicates the median; the box indicates the upper and lower quartiles and the whiskers indicate the 5th and 95th percentiles of the data. Plant functional types were defined according to the IGBP classification, including SAV (savannas); SHR (shrublands); ENF (evergreen needleleaf forests); EBF (evergreen broadleaf forests); DBF (deciduous broadleaf forests); MF (mixed forests); GRA (grasslands) and CRO (croplands). Climate types were defined according to the Köppen-Geiger classification as in Migliavacca *et al*. (*65*): Tropical (Aw, Af, Am), Dry (BSh, BSk, BWh), Sub-Tropical (Cfa, Csa, Csb, Cwa), Temperate (Cfb), Continental (Dfa, Dfb, Dwa, Dwb, Dwc), and Boreal (Dfc, Dsc).

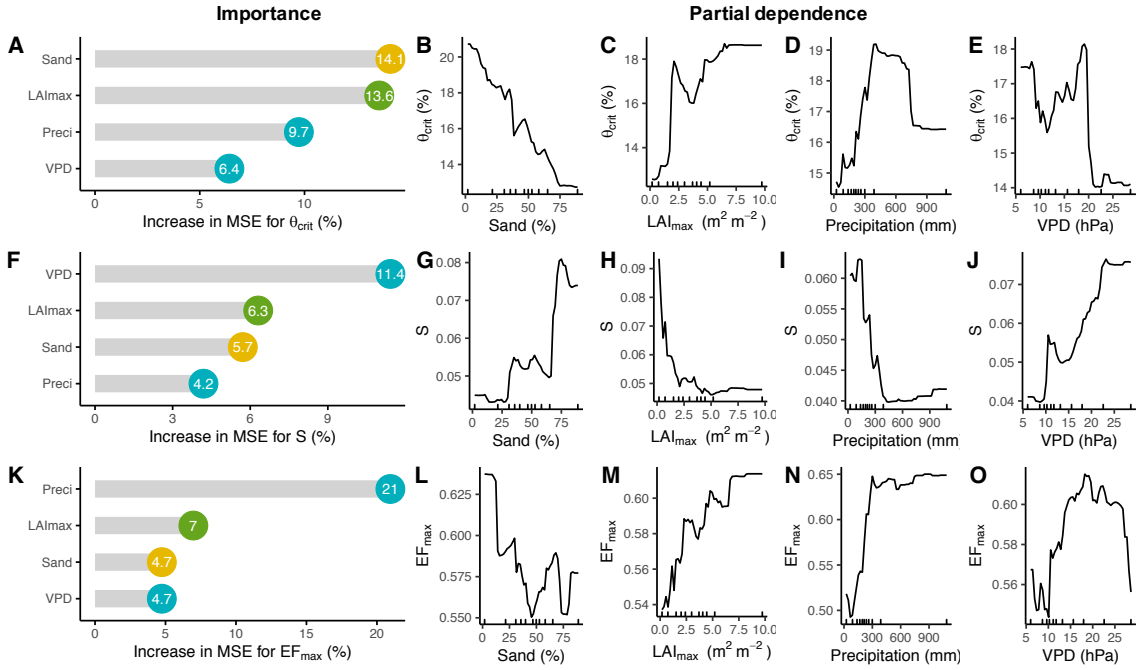

Fig. 3. Importance of soil, vegetation structure and climate properties and partial dependence. Predictive relative importance for θ_{crit} (A), S (F) and EF_{max} (K). Numbers in the circles represent the percentage increase in mean squared error (MSE). Yellow circles represent soil variable; green circles represent vegetation structure variable; light blue circles represent climate variables. Partial dependence plots of the predictors for θ_{crit} (B-E), S (G-J) and EF_{max} (L-O). The slopes of the partial dependence plot indicate the sensitivity of the response variable to the specific predictor. Sand: sand fraction (%); LAI_{max}: maximum leaf area index (m^2 m^{-2}); VPD: mean VPD during the peak growing season (hPa); Preci: total precipitation amount during the peak growing season (mm). Tick marks in the x axis represent the minimum, maximum and deciles of the variable distribution.

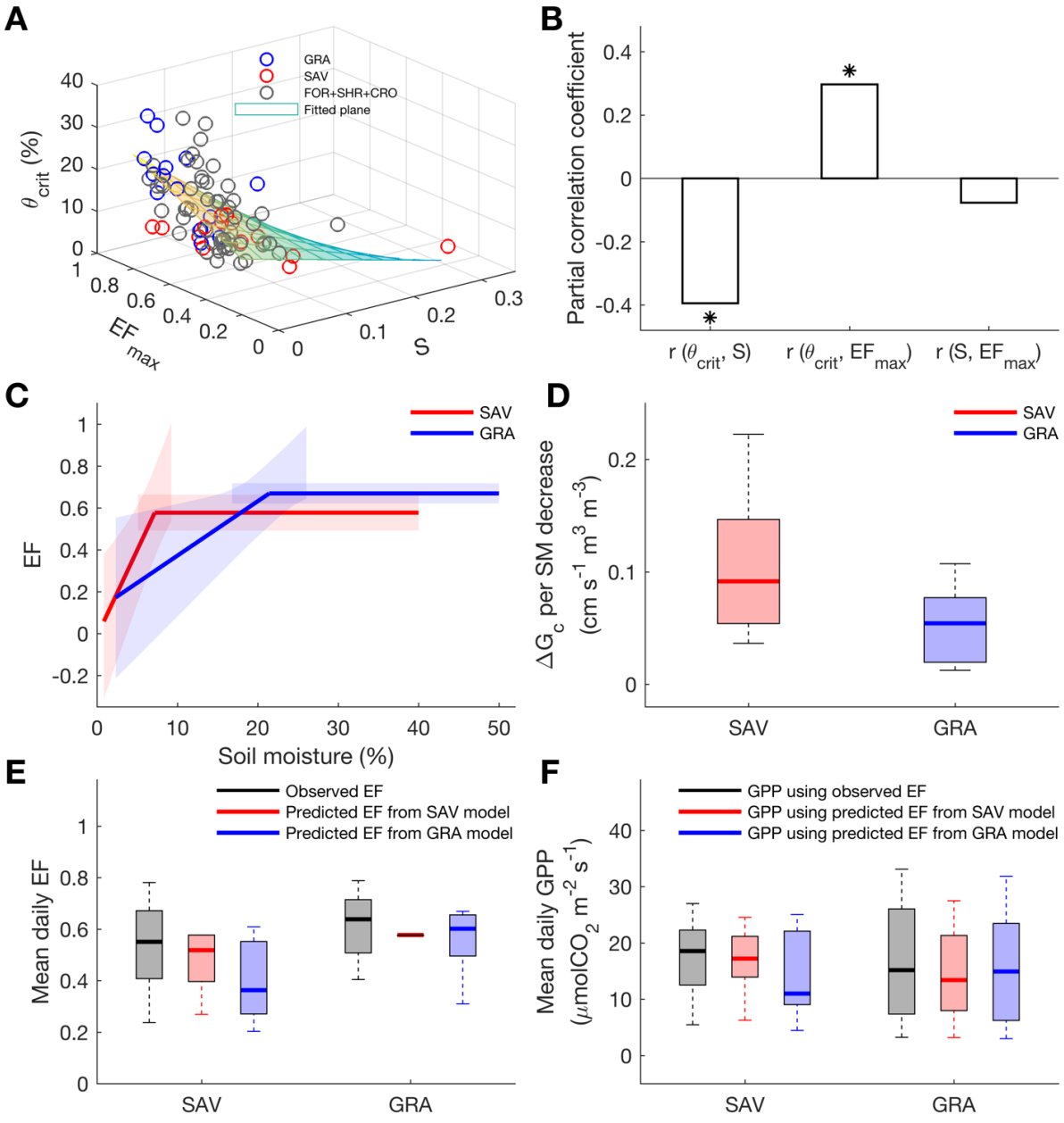

Fig. 4. Relationships between θ_{crit}, S and EF_{max} and the optimal adaptation of local EF–SM response function. The distribution of θ_{crit}, S and EF_{max} across all sites in different biomes (A). Partial correlation between θ_{crit}, S and EF_{max} across all sites (B). The mean response functions of EF–SM in savannas and grasslands (C), while the shading bounds the 95% confidence interval. The canopy conductance (G_c) change rates per SM decrease during water-limited stage in savannas and grasslands (D). Observed and predicted mean daily EF during the peak growing season in savannas and grasslands by swapping two response functions of EF–SM, the one from savannas and the one from grasslands (E). Calculated mean daily GPP during the peak growing season in savannas and grasslands using observed and predicted EF from two response functions of EF–SM (F). For each box plot, the middle line indicates the median; the box indicates the upper and lower quartiles, and the whiskers indicate the 5th and 95th percentiles of the data. GRA: grasslands; SAV: savannas; FOR: forests; SHR: shrublands; CRO: croplands.

Supplementary Materials

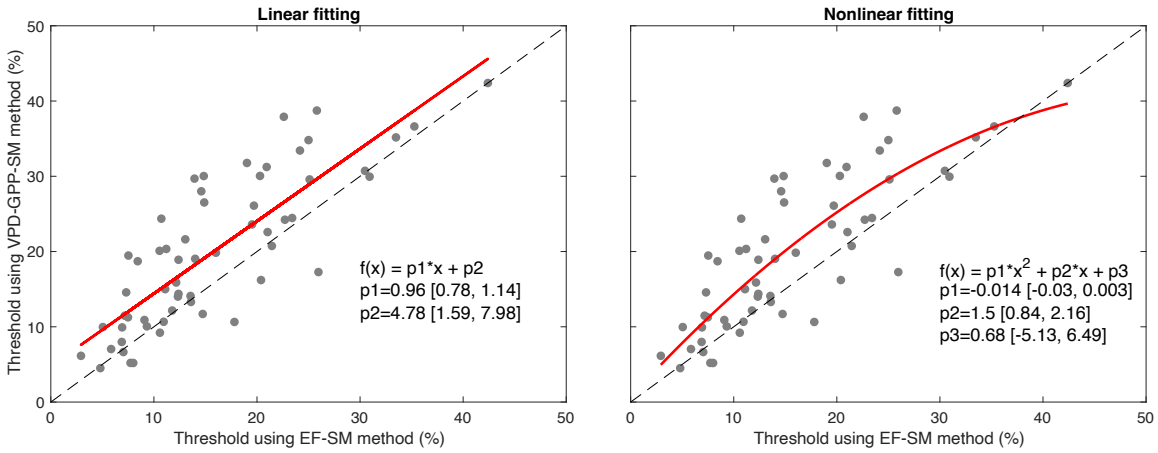

Fig. S1. Fitting the soil moisture thresholds from EF–SM method and VPD–GPP–SM method using linear ($f(x) = p1 \times x + p2$) and nonlinear ($f(x) = p1 \times x^2 + p2 \times x + p3$) functions. The 95% confidence intervals are shown in parenthesis.

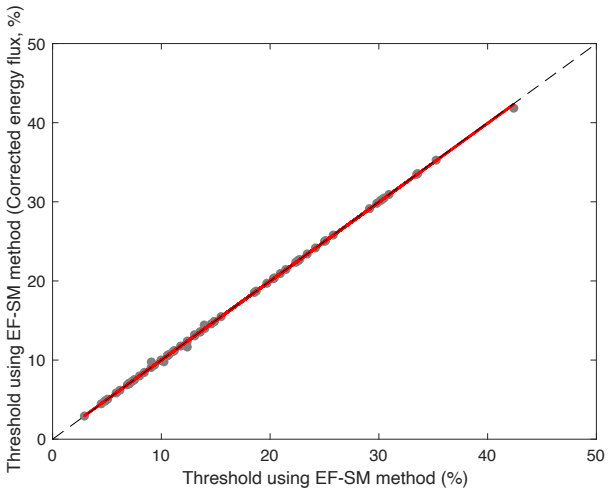

Fig. S2. The effect of different energy fluxes (LE and H vs. LE.CORR and H.CORR) on SM thresholds estimated from EF–SM method across all sites with corrected energy fluxes. Both the 'LE' (or 'H') and 'LE.CORR' (or 'H.CORR') variables were reported by the FLUXNET database for latent (or sensible) energy exchange. LE.CORR and H.CORR are the "energy balance corrected" version of latent and sensible heat flux, based on the assumption that the Bowen ratio is correct.

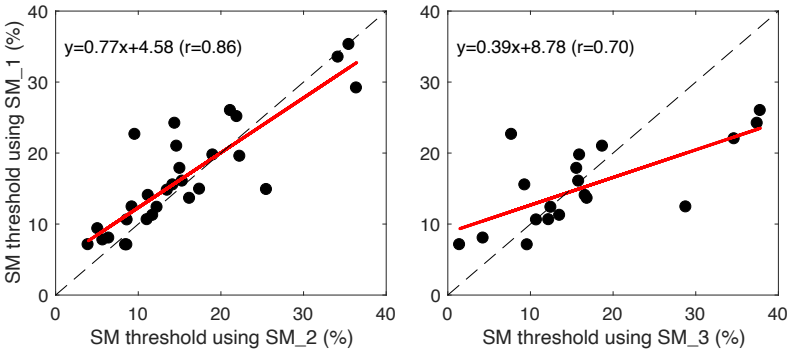

Fig. S3. Relationships between estimated SM thresholds using the SM in the first depth (SM_1) and the SM in second (SM_2) or third depth (SM_3) provided by each research site.

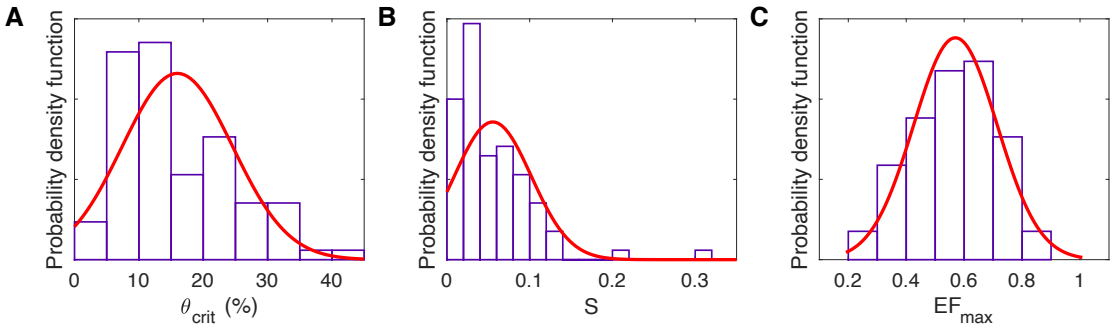

Fig. S4. Probability distributions of θ_{crit}, S and EF_{max} across all sites (A-C).

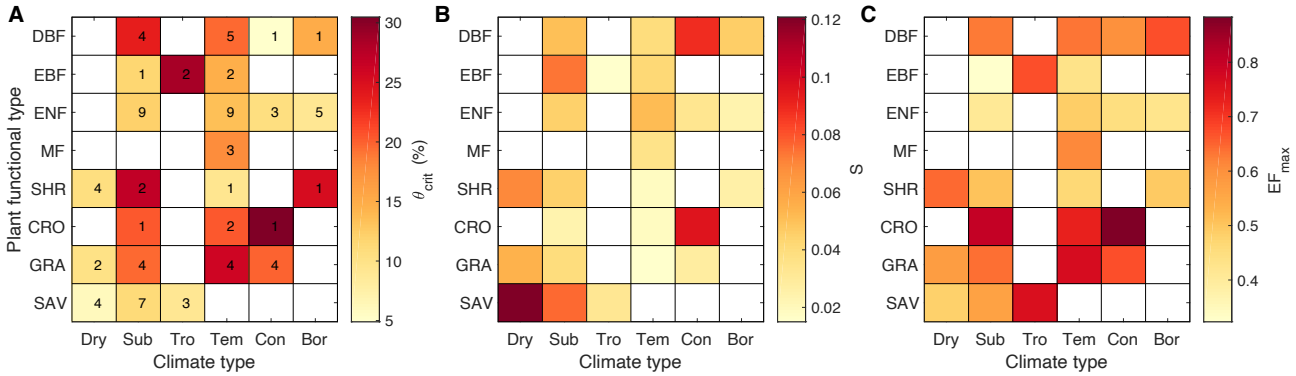

Fig. S5. Values of θ_{crit}, S and EF_{max} in a matrix of plant functional types and climate types. The number in the first panel indicates the number of sites in each bin. SAV: savannas; SHR: shrublands; ENF: evergreen needleleaf forests; EBF: evergreen broadleaf forests; DBF: deciduous broadleaf forests; MF: mixed forests; GRA: grasslands; CRO: croplands. Sub: sub-tropical; Tro: tropical; Tem: temperate; Con: continental; Bor: boreal.

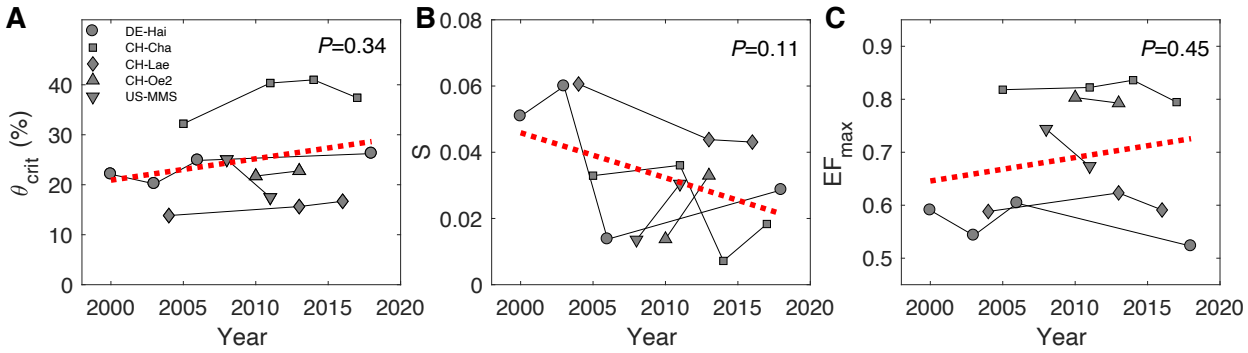

Fig. S6. The temporal change of θ_{crit}, S and EF_{max} at five sites with at least 15 years of measurements (A-C). The red line represents the linear fitting over all site-years. Different sites were shown in different marks. *P* values indicate statistical significance of the linear trend.

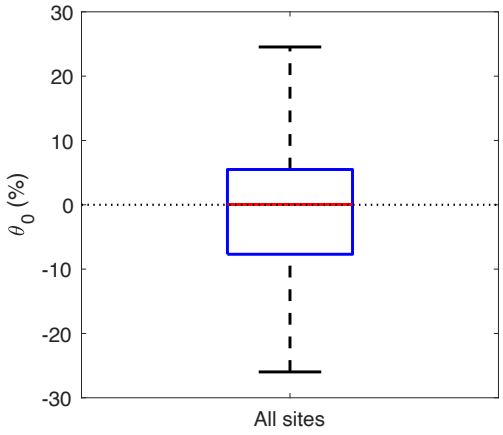

Fig. S7. Values of θ_0 (the value of SM at which EF equals zero) across sites. The θ_0 is not significantly differ from zero ($P > 0.05$).

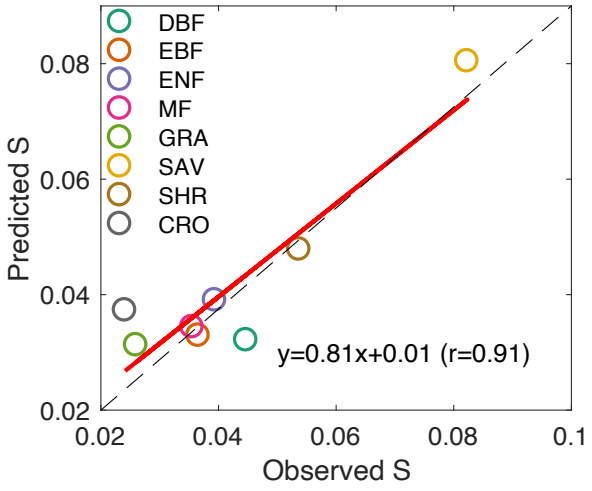

Fig. S8. The relationship between observed and predicted S across biomes.

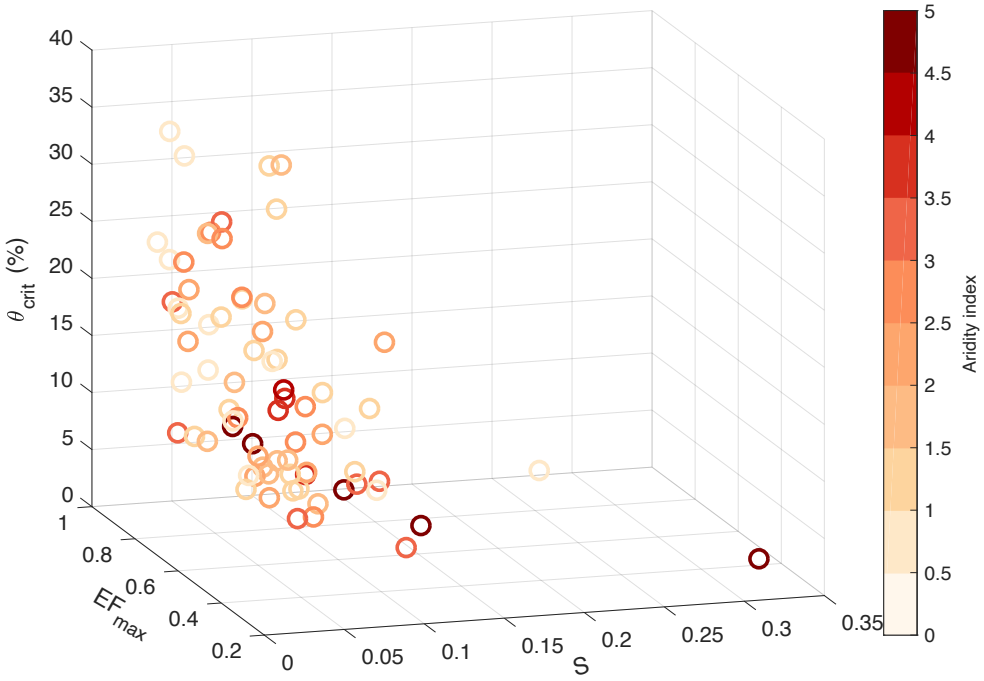

Fig. S9. The distribution of θ_{crit}, S and EF_{max} across all sites with aridity index.

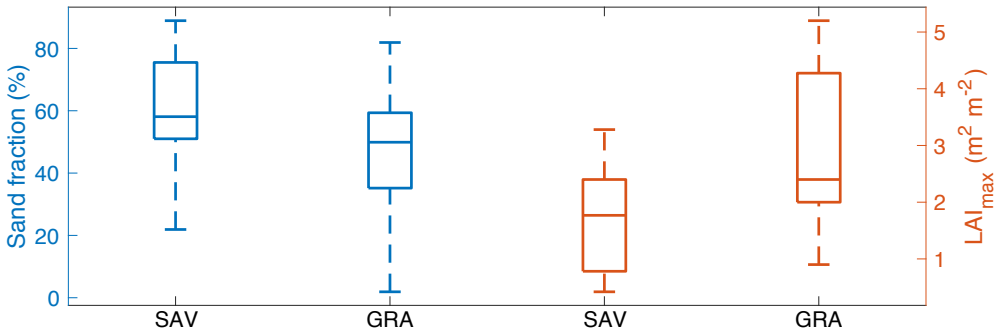

Fig. S10. Sand fraction and maximum leaf area index (LAI_{max}) in savannas and grasslands. Both sand fraction and LAI_{max} in savannas (SAV) and grasslands (GRA) are significantly different (Kruskal-Wallis test, $P < 0.05$). For each box plot, the middle line indicates the median; the box indicates the upper and lower quartiles, and the whiskers indicate the 5th and 95th percentiles of the data.

Table S1. Eddy covariance sites used in this study. Site identifier (ID), latitude (Lat, °), longitude (Long, °), plant functional type (PFT), climate type, and study periods are listed. Plant functional types were defined according to the IGBP classification, including SAV (savannas); SHR (shrublands); ENF (evergreen needleleaf forests); EBF (evergreen broadleaf forests); DBF (deciduous broadleaf forests); MF (mixed forests); GRA (grasslands) and CRO (croplands). Climate types were defined according to the Köppen-Geiger classification.

Site ID	Lat	Long	PFT	Climate	Periods
AU-ASM	-22.28	133.25	SAV	bsh	2010-2014
AU-Cpr	-34.00	140.59	SAV	bsk	2010-2014
AU-DaS	-14.16	131.39	SAV	aw	2008-2014
AU-Dry	-15.26	132.37	SAV	aw	2008-2014
AU-Gin	-31.38	115.71	SAV	csa	2011-2014
AU-How	-12.49	131.15	SAV	aw	2001-2014

AU-Rig	-36.65	145.58	GRA	cfb	2011-2014
AU-Whr	-36.67	145.03	EBF	cfb	2011-2014
AU-Wom	-37.42	144.09	EBF	cfb	2010-2014
BE-Bra	51.31	4.52	MF	cfb	2012-2019
BE-Maa	50.98	5.63	SHR	cfb	2016-2020
CA-Ca2	49.87	-125.29	ENF	cfb	1999-2010
CA-Ca3	49.53	-124.90	ENF	cfb	2001-2010
CA-NS6	55.92	-98.96	SHR	dfc	2001-2005
CA-Oas	53.63	-106.20	DBF	dfc	1997-2010
CA-Qfo	49.69	-74.34	ENF	dfc	2003-2010
CA-SF2	54.25	-105.88	ENF	dfc	2001-2006
CA-SJ2	53.95	-104.65	ENF	dfc	2002-2010
CA-TP1	42.66	-80.56	ENF	dfb	2002-2014
CA-TPD	42.64	-80.56	DBF	dfb	2012-2014
CH-Cha	47.21	8.41	GRA	cfb	2005-2020
CH-Dav	46.82	9.86	ENF	cfb	2006-2014
CH-Lae	47.48	8.37	MF	cfb	2004-2020
CH-Oe1	47.29	7.73	GRA	cfb	2002-2008
CH-Oe2	47.29	7.73	CRO	cfb	2004-2018
CN-Cng	44.59	123.51	GRA	dwa	2007-2010
CN-Dan	30.50	91.07	GRA	dwc	2004-2005
CN-Du2	42.05	116.28	GRA	dwb	2006-2008
CN-Du3	42.06	116.28	GRA	dwb	2009-2010
CN-Qia	26.74	115.06	ENF	cfa	2003-2005
CZ-Lnz	48.68	16.95	MF	cfb	2015-2020
CZ-RAJ	49.44	16.70	ENF	cfb	2012-2018
DE-Gri	50.95	13.51	GRA	cfb	2007-2020
DE-Hai	51.08	10.45	DBF	cfb	2000-2020
DE-HoH	52.09	11.22	DBF	cfb	2015-2020
DE-Hzd	50.96	13.49	DBF	cfb	2010-2020
DE-Kli	50.89	13.52	CRO	cfb	2005-2018
DE-Lnf	51.33	10.37	DBF	cfb	2002-2012
DE-Obe	50.79	13.72	ENF	cfb	2008-2020
ES-Abr	38.70	-6.79	SAV	csa	2015-2018
ES-LM1	39.94	-5.78	SAV	csa	2014-2020
ES-LM2	39.93	-5.78	SAV	csa	2014-2020
FR-Bil	44.49	-0.96	ENF	cfb	2014-2020
FR-Hes	48.67	7.06	DBF	cfb	2014-2020
FR-LBr	44.72	-0.77	ENF	cfb	1996-2008
GF-Guy	5.28	-52.92	EBF	am	2004-2014
IT-BFt	45.20	10.74	DBF	cfa	2019-2020
IT-CA1	42.38	12.03	DBF	csa	2011-2014
IT-Col	41.85	13.59	DBF	csa	2006-2014

IT-Cpz	41.71	12.38	EBF	csa	1997-2009
IT-Lsn	45.74	12.75	SHR	cfa	2016-2020
IT-Noe	40.61	8.15	SHR	csa	2004-2014
IT-SRo	43.73	10.28	ENF	csa	1999-2012
MY-PSO	2.97	102.31	EBF	af	2003-2009
NL-Loo	52.17	5.74	ENF	cfb	1999-2016
RU-Fyo	56.46	32.92	ENF	dfb	2007-2017
SE-Htm	56.10	13.42	ENF	cfb	2015-2020
SE-Nor	60.09	17.48	ENF	dfb	2014-2020
SE-Ros	64.17	19.74	ENF	dfc	2014-2020
SN-Dhr	15.40	-15.43	SAV	bwh	2010-2013
US-AR1	36.43	-99.42	GRA	cfa	2009-2012
US-Dk1	35.97	-79.09	GRA	cfa	2001-2008
US-Dk3	35.98	-79.09	ENF	cfa	2001-2008
US-FR2	29.95	-98.00	SAV	cfa	2005-2008
US-Fmf	35.14	-111.73	ENF	csb	2005-2010
US-Fuf	35.09	-111.76	ENF	csb	2005-2010
US-GLE	41.37	-106.24	ENF	dfc	2004-2014
US-Goo	34.25	-89.87	GRA	cfa	2002-2006
US-MMS	39.32	-86.41	DBF	cfa	1999-2014
US-Me1	44.58	-121.50	ENF	csb	2004-2005
US-Me3	44.32	-121.61	ENF	csb	2004-2009
US-Me4	44.50	-121.62	ENF	csb	1996-2000
US-Me6	44.32	-121.61	ENF	csb	2010-2014
US-Rls	43.14	-116.74	SHR	bsh	2014-2017
US-Rms	43.06	-116.75	SHR	bsh	2014-2017
US-Ro5	44.69	-93.06	CRO	dfa	2017-2017
US-SRG	31.79	-110.83	GRA	bsk	2008-2017
US-SRM	31.82	-110.87	SAV	bsk	2004-2014
US-Sta	41.40	-106.80	SHR	bsh	2005-2009
US-Ton	38.43	-120.97	SAV	csa	2001-2014
US-Tw3	38.12	-121.65	CRO	csa	2013-2014
US-Var	38.41	-120.95	GRA	csa	2001-2014
US-Whs	31.74	-110.05	SHR	bsk	2007-2014
US-Wkg	31.74	-109.94	GRA	bsk	2004-2014
ZA-Kru	-25.02	31.50	SAV	cwa	2000-2013

973

Table S2. Temporal dynamics of θ_{crit}, S and EF_{max} at DE-Hai. The standard error values are shown in parenthesis. NA means no θ_{crit} estimated.

Year	θ_{crit}	S	EF_{max}
2000-2002	22.10 (0.59)	0.05 (0.01)	0.59 (0.01)
2003-2005	20.17 (0.47	0.06 (0.01)	0.54 (0.01)
2006-2008	24.86 (2.06)	0.01 (0.01)	0.60 (0.01)
2009-2011	*NA*	*NA*	*NA*
2012-2014	*NA*	*NA*	*NA*
2015-2017	*NA*	*NA*	*NA*
2018-2019	26.23 (1.28)	0.03 (0.004)	0.52 (0.02)
Mean	23.34 (1.36)	0.04 (0.01)	0.56 (0.02)
2000-2019	24.17 (0.46)	0.03 (0.003)	0.55 (0.01)